

# Detecting Extrasolar Planets with Integral Field Spectroscopy

A. Berton<sup>1</sup>, R. G. Gratton<sup>2</sup>, M. Feldt<sup>1</sup>, T. Henning<sup>1</sup>, S. Desidera<sup>2</sup>, M. Turatto<sup>2</sup>,  
H. M. Schmid<sup>3</sup> and R. Waters<sup>4</sup>

berton@mpia.de, gratton@pd.astro.it, feldt@mpia.de, henning@mpia.de,  
desidera@pd.astro.it, turatto@pd.astro.it, schmid@astro.phys.ethz.ch,  
rensw@science.uva.nl

Received \_\_\_\_\_; accepted \_\_\_\_\_

---

<sup>1</sup>Max-Planck-Institut für Astronomie (MPIA), Königstuhl 17, D-69117, Heidelberg, Germany

<sup>2</sup>Osservatorio Astronomico di Padova INAF, Vic. Osservatorio 5, I-35122, Padova, Italy

<sup>3</sup>Institute of Astronomy, ETH Zentrum, 8092 Zurich, Switzerland

<sup>4</sup>Astronomical Institute, University of Amsterdam, Kruislaan 403, 1098 SJ Amsterdam,  
The Netherlands

## ABSTRACT

Observations of extrasolar planets using Integral Field Spectroscopy (IFS), if coupled with an extreme Adaptive Optics system and analyzed with a Simultaneous Differential Imaging technique (SDI), are a powerful tool to detect and characterize extrasolar planets directly; they enhance the signal of the planet and, at the same time, reduces the impact of stellar light and consequently important noise sources like speckles. In order to verify the efficiency of such a technique, we developed a simulation code able to test the capabilities of this IFS-SDI technique for different kinds of planets and telescopes, modelling the atmospheric and instrumental noise sources. The first results obtained by the simulations show that many significant extrasolar planet detections are indeed possible using the present 8m-class telescopes within a few hours of exposure time. The procedure adopted to simulate IFS observations is presented here in detail, explaining in particular how we obtain estimates of the speckle noise, Adaptive Optics corrections, specific instrumental features, and how we test the efficiency of the SDI technique to increase the signal-to-noise ratio of the planet detection. The most important results achieved by simulations of various objects, from  $1 M_J$  to brown dwarfs of  $30 M_J$ , for observations with an 8 meter telescope, are then presented and discussed.

*Subject headings:* Instrumentation: miscellaneous - Techniques: spectroscopic - Planetary systems

## 1. Introduction

At present, around 150 extrasolar planets have been found around stars other than the Sun<sup>1</sup>. Nearly all of them have been detected in indirect ways, generally by observing the effects of gravitational perturbations of the host star due to the presence of the companion. These perturbations can be measured by radial velocity changes or precise astrometry. In addition, transits and microlensing have been successfully applied to detect planets. Direct detections of extrasolar planets, with the present technology available, are still a challenging goal to achieve. Only recently the first observations of the signals coming directly from planetary mass objects have been possible, in some particular cases of young companions around low-mass stars or brown dwarfs (for example see Chauvin et al. 2004); but in general the detection of Jupiter-like planets around Solar-type stars remains a challenge. Difficulties in direct detection of faint companions arise from the complex structure of the stellar Point Spread Function (PSF) which swamps the light of the planet. This stellar halo is usually brighter than the planet at every wavelength, and it is also a source of noise, in particular the speckle noise.

In Sec.2 it is explained why atmospheric speckles are the most important source of noise that we have to consider in direct detections of planets. Thus, an efficient method for speckle noise reduction is required. Here we suggest a Simultaneous Differential Imaging technique (SDI) applied to IFS observations of the star-planet system, as described in Sec.3. In order to test the capability of such a technique in reducing speckle noise and detecting planets, we developed a dedicated piece of software, presented in Sec.4, that aims to simulate as accurately as possible an observation of an extrasolar planet using an IFS. From the analysis of the results of the simulations, it has been possible to understand which

---

<sup>1</sup>See for example the continuously updated Extrasolar Planet Encyclopedia web site ([www.obspm.fr/encycl/encycl.html](http://www.obspm.fr/encycl/encycl.html)) and references to published papers therein.

kinds of planets are really detectable and characterizable for various telescope diameters, e.g. an 8m-class telescope. Some encouraging results of these simulations are presented in Sec.5.

## 2. The speckle noise

For ground-based observations, speckles are mainly due to atmospheric turbulence and they result from the interference of light from many coherent patches of typical diameter  $r_0$  (called the “Fried radius”), distributed over the full aperture of the telescope. A detailed description of the formation of speckles can be found in Racine et al. (1999). Speckles look like bright spots of typical Full Width Half Maximum (FWHM)  $\sim \lambda/D$  radians, where  $\lambda$  is the wavelength and  $D$  is the diameter of the telescope aperture. The number of speckles per unit area, in case of  $D \gg r_0$  (Roddier et al. 1982) is:

$$n_s \simeq \frac{0.342}{\pi (\lambda/D)^2}. \quad (1)$$

This means that the larger the diameter of the telescope, the higher the number of speckles. The spatial distribution of speckles, the so-called speckle pattern, is a direct consequence of the wavefront corrugation by atmospheric turbulence and optical imperfections. Hereafter we will focus our attention on speckles due to the atmosphere. The atmospheric speckle lifetime, called “coherence time”  $\tau_0$ , is proportional to  $r_0/\Delta v$ , where  $\Delta v$  is the velocity dispersion in the turbulent seeing layers across the telescope line of sight. This speckle variability, related to the variability of the wavefront corrugation, results in “speckle boiling” and is the source of speckle noise.

The statistics of speckle noise variance are not very simple, because the speckles are not independent events by the nature of the interference that produces them. In the presence

of an Adaptive Optics system (AO) for compensating atmospheric turbulence, Racine et al. (1999) found, for the speckle variance in the PSF halo, the expression:

$$var(speckles) \simeq 1.7\pi \left[ \left( \frac{\lambda}{D} \right)^2 (1 - S) F_* f_{halo}(\theta) \right]^2 \frac{\tau_0}{t}, \quad (2)$$

where  $F_*$  is the total flux from the star,  $f_{halo}$  indicates the radial profile of the PSF halo ( $\theta$  is the angular distance from the center),  $t$  is the exposure time and  $S$  is the Strehl ratio given by the AO compensation. Since  $F_*$  is proportional to the exposure time  $t$ , this equation shows that the variance of speckles is proportional to  $t$ . This variance can actually be reduced in case of an AO system able to reach very high Strehl ratios  $S$ .

Considering the variance of the photon noise of the PSF halo, which is

$$var(photons) = \pi \left( \frac{\lambda}{D} \right)^2 (1 - S) F_* f_{halo}(\theta), \quad (3)$$

a comparison between the two variances shows that the speckle one is usually much larger than the photonic one.<sup>2</sup>

We can conclude that the speckles are the most important source of noise that we have to face searching directly for extrasolar planets from the ground, and we must find a way for reducing them. Obviously, the best solution would be space telescopes, outside the terrestrial atmosphere: see e.g. the projects DARWIN (Fridlund 2002) and Terrestrial Planet Finder (TPF, Beichman et al. 1999); even so, because of the complexity of a space

---

<sup>2</sup>A separate discussion has to be done for long-time speckles, or “super-speckles”, which are more related to static aberrations than to the atmosphere. It is not easy to determine their life time, that will be much longer than  $\tau_0$ : in the worst case, they don’t change during all the integration time.

mission, to exploit new ways for speckle noise reduction for ground-based observations is not a worthless effort. From equation 2, it is clear that an extreme AO system is mandatory in order to reduce dramatically the speckle intensity: AO systems can reduce seeing disk and get a sufficient spatial resolution for our investigation, and at the same time can improve the value of the Strehl ratio  $S$ . Present AO systems are able to reach very high Strehl ratios (up to 0.7 at  $\lambda=2.2\mu\text{m}$ ) but they are still far from being perfect ( $S=1$ ). Still after AO correction, speckle noise is orders of magnitude larger than the photon noise; therefore the reduction of the speckle noise to a level comparable to the photon noise can be achieved only using additional techniques.

Many different methods have been suggested, almost all of them based on a combination of XAO and coronography. In fact, the coronograph can improve the sensitivity of an imaging system to faint structures surrounding the bright source (Sivaramakrishnan et al. 2001). In addition, noise can be reduced using a narrow-band coronographic interferometer (Codona & Angel 2004), nulling interferometry (Bracewell 1978; Woolf & Angel 1998), adaptive holograms for removing coronographic residues (Labeyrie 2004) or synchronous interferometric speckle subtraction (Guyon 2004). The polarization of the light reflected by the planet can be also used to reduce the effect of speckles (Baba & Murakami 2003; Stam et al. 2004). A large improvement in planet detection, in particular for Earth-like planets, can be reached by a combination of AO, coronography and Extremely Large Telescopes (ELTs) because of the large amount of photons collectible in short exposures (Chelli 2005; Sivaramakrishnan & Yaitskova 2005).

### 3. The IFS-Simultaneous Differential Imaging technique

The main idea behind SDI is to use differential measurements in two bands, only one of them containing the planet signal, to enhance the features that make the planet

distinguishable from the central star (see, e.g., Smith 1987; Rosenthal et al. 1996; Racine et al. 1999; Marois et al. 2000). Practically this can be done choosing a couple (or more) wavelengths at which the light of the star presents very small differences in intensity, but at the same time the light of the planet is changing drastically because of absorption bands<sup>3</sup>. The wavelengths must be chosen appropriately for each kind of target. In the case of low-mass brown dwarfs or gaseous giant planets, for instance, the methane absorption bands in the near-infrared are the best solution (see Sec.3.1 for details). The simultaneous observation of the star-planet system at two wavelengths on and off the methane absorption band, done using special narrow-band filters e.g. in NACO-SDI on ESO’s VLT (Lenzen et al. 2004), gives a set of images that, after a suitable re-scaling in wavelength, can be combined using various algorithms in order to subtract the stellar light (see e.g. Biller et al. 2006a,b). Because of the simultaneity of the observations, the subtraction of the stellar light leads also to the subtraction of speckles and the reduction of the speckle noise. A recent example of a low mass companion (a cool methane rich brown dwarf) using NACO-SDI is described in Biller et al. (2006c).

Although SDI was originally proposed for two wavelengths only and for a simple difference operation, Marois et al. (2000) showed that the speckle noise reduction can be much more efficient if observations at 3 wavelengths are available, using a “double-difference”. Starting from here, it is reasonable to assume that a larger number of images at different wavelengths, taken with a small regular spectral separation, can result in even better reduction of speckle noise. This idea suggested the use of an integral field spectrograph for collecting data simultaneously at a large number of different wavelengths, given by the total spectral length and the spectral resolution of the disperser. IFS is

---

<sup>3</sup>A similar approach is also possible in polarimetry, exploiting the fact that light reflected by a planet is partially polarized (Stam et al. 2004).

preferable to a single slit spectrograph, because it allows the detection of the companion even if its position is unknown. Moreover, an IFS has some advantages with respect to a filter-based SDI in reducing speckle noise and in increasing the signal-to-noise ratio of the detection, because of the possibility to analyze a larger amount of information at many different wavelengths, and these advantages are discussed in detail in Sec.6.1. There is however a disadvantage to using this technique owing to the instrumental complexity and complicated data reduction procedure.

### 3.1. The stellar and planetary spectra

To design an instrument dedicated to the detection of planets using the IFS-SDI technique, it is necessary to have a clear idea of the spectral features that will be observed, in order to choose the best spectral region for observations, and to optimize the spectral resolution and spectral coverage of the instrument. In this section, we discuss these aspects of the observation of giant Jupiter-like planets around solar-type stars.

Models of giant planets, like those of Burrows et al. (2004) for irradiated planets and Burrows et al. (2003) for isolated objects, clearly show that the most interesting features expected in the spectra are the broad absorption bands of water and methane in the near-infrared. These bands can be studied at very low spectral resolution (15 or 30, see Fig.1). From these plots we can see that the methane dominated spectra are characterized by “emission peaks”, the portions of spectrum not affected by absorptions, which are expected to be constant in wavelength, but their intensities are expected to change from object to object. At the same resolution and in the same spectral region the spectrum of a solar-type star is nearly featureless and may be fitted by a polynomial curve (see Fig.2). The combination of strong planetary features and very smooth stellar spectra makes this spectral region optimal for application of the SDI technique, which is sensitive to the

variations in contrast between star and planet.

#### 4. Description of the simulation code

The simulation code presented in this section is called CSP (CHEOPS Simulation Program) and has been developed in the context of the CHEOPS project (CHaracterizing Exo-planets by Opto-infrared Polarimetry and Spectroscopy, Feldt et al. 2005). This project was born as an answer to ESO’s call for a “Planet Finder” at the VLT. The concept of this instrument was based on an extreme adaptive optics system combined with two scientific channels. The first channel is a polarization analyzer based on ZIMPOL (Povel 1998; Gisler et al 2004); the second channel is an IFS, based on the SAURON concept (Bacon et al. 2001) but adapted to the diffraction limit case relevant to detection of extrasolar giant planets. This IFS consists of a microlens array composed of  $254 \times 254$  hexagonal microlenses covering a field of view of  $3''.5 \times 3''.5$ . The disperser is an Amici prism, which can give spectra with a nearly constant resolution of  $R=15$  in the spectral region between 0.9 and  $1.7\mu\text{m}$ . The resolution has been chosen in order to allow the investigation of the broad methane absorption bands, and at the same time to sample all the requested spectral range with a few pixels on the detector (length of  $\sim 20$  pixels). This length, the resolution and the microlens pitch ( $0''.0138$ ) have been chosen in order to allow a very low level of cross-talk between spectra ( $\geq 10^{-4}$ )<sup>4</sup>. It is important to note that in the CHEOPS design we have only two refractive elements before the IFS, which are an Atmospheric Dispersion Corrector (ADC), included in the AO system, and a dichroic beam splitter: since these two elements

---

<sup>4</sup>The resolution of 15 has been chosen also to optimize the contrast between the spectral features we want to observe (molecular bands like methane) and the length of the spectra on the detector.

don't contribute in a relevant way to chromatic aberrations (the latter has no optical power, the former is composed by flat surfaces), then the total chromatic error is considered to be negligible. A detailed description of the CHEOPS IFS can be found in Claudi et al. (2004).

Starting from the technical definitions of CHEOPS, we developed a code with the goal of simulating observations of extrasolar planets using an extreme AO-assisted IFS, focusing our attention on the sources of noise affecting these observations. In particular, an accurate simulation of the dominant speckle noise was required, beside all the detector noise sources, instrumental aberrations and so on. Simulated observation can then be used to test the efficiency of IFS-SDI for finding planets and to understand exactly which kind of object can be actually detected with such an instrument.

An interesting aspect of this simulation code is the possibility to allow simulations of different kinds of telescopes and different technical configurations. The code can be used for simulating observations with both an 8 meter telescope and an ELT. It can also be adapted, knowing the appropriate spectral features, to the detection of earth-like planets rather than hot and cold Jupiters. In this paper we focus our attention on the results related to the case of an 8 meter telescope and Jupiter-like planets: the case of ELTs and Earth-like planets will be exploited in a forthcoming paper.

A large number of input parameters of different nature are required by the simulation code. In order to simulate the AO correction all relevant parameters describing the atmospheric turbulence must be defined ( $r_0$ ,  $\tau_0$ , etc.). In addition, the diameter of the telescope and the optical path of the instrument has to be known as well as the expected static aberrations. The shape, the focal length and the expected scattered light given by the microlenses has to be considered. Finally, the detector features strongly affect the final signal-to-noise ratio. The output given by the simulation code is a single image, on which all the spectra produced by the IFS are present, showing the spectra of the star and, usually

hidden, the spectra of a given number of planets.

#### 4.1. Simulation of atmospheric turbulence and AO correction

Data concerning atmospheric turbulence, telescope vibration and Adaptive Optics correction are elaborated as a set of images, phase screens, which represents the wavefronts associated with observations provided by AO. A phase screen of the atmospheric turbulence is produced defining the spatial properties of the screen by a von Kármán spectrum, using a procedure based on Lane et al. (1992). A single layer atmosphere was simulated corresponding to seeing conditions of  $0''.6$ ,  $0''.85$  and  $1''.0$  at  $\lambda = 550$  nm.  $\tau_0$  was always 0.01 s. Telescope vibrations were added as time-dependent tip and tilt terms at 14 Hz and 48 Hz with amplitudes typical for the VLT; an ADC is supposed to be present within the AO system. As this paper is not concerned with the details of the AO system, a very simple AO simulation technique was adopted where the wavefront sensor is simulated by re-sampling the input wavefront itself to the sensor resolution of 40 apertures across the 8.0 m primary mirror. This corresponds exactly to the number and geometry of the actuators in the assumed deformable mirror. The “sensor” information was fed into the control loop which uses a simple integrator controller running at a loop speed 2 kHz. This controller produces another  $40 \times 40$  matrix which represent the mirror commands. Since it is still in the same units as the wavefront itself, the rest of the system is simulated simply by re-expanding this  $40 \times 40$  matrix to the original spatial scale of the wavefront and subtracting it from the input phase screen appropriate for the moment in time when the mirror signals are applied.

Simulating AO in this way we do not include specific effects of certain wavefront sensor types and other specialities, but we do get a rather optimistic estimate what an XAO system could achieve on an 8 m telescope. The resulting Strehl ratios vary between 0.4 and 0.8. It should be noted that with this technique we do see a strong dependence of

planet detectabilities from seeing values (see Sec.5.5), but since the AO simulation is not really detailed, one should rather assume the Strehl number as the input variable of that dependency. How the Strehl ratio depends on seeing has to be determined in detailed AO simulations not included in this work. On the output side of the atmosphere-AO simulation chain, every phase screen represents the wavefront at a precise moment of the observation and it is related to a very short interval of time. This interval is shorter than the coherence time of the turbulence. Each screen differs slightly from the previous one. Phase screens are monochromatic, but they can easily be converted to the required wavelength using appropriate scale factors.

#### 4.2. Creation of the PSF and the speckle patterns

Given a phase screen and the entrance pupil of the telescope, the code transforms the phase screen, a measure of phase  $\phi$ , in an electric field  $E = Ae^{i\phi}$ , where the amplitude  $A$  is given by the pupil and  $\phi$  by the phase screen. The PSF related to that screen is obtained using a Fourier Transform:

$$psf = FT(E) = \iint_{-\infty}^{+\infty} E(x, y) e^{-i2\pi(f_x x + f_y y)} dx dy, \quad (4)$$

where  $f_x$  and  $f_y$  are the coordinates in frequency space.

We simulated a simplified model of Lyot coronograph, in order to avoid the saturation of the central peak. Such a coronograph would also be useful in reducing the effects of diffraction rings and patterns. It is included by applying on the focal plane a central obscuration (with a diameter of 0.55 arcseconds at the shortest wavelength) covering the central stellar peak, and then a Lyot mask on the pupil plane. This has been modeled as an aperture on the pupil plane with transmission equal to 1 within 95% of the diameter of

the pupil of the telescope, and it is slightly apodized beyond this value using a gaussian function. All these choices have been totally arbitrary because the final configuration of the coronograph for IFS has been not decided yet. When a definitive coronograph will be chosen, we will be able to improve the simulation of this part of the code. For the moment, we stick with this simplified model.

This PSF has been obtained from a single phase screen. Therefore, it is related to a short interval of time and it will be characterized by an instantaneous speckle pattern. In order to simulate a longer exposure time we perform a suitable number of repeats and sum the resulting PSFs into one.

Our code convolves this PSF with an “object” image that is a set of point-like sources, the star and one or more planets, characterized by different intensities. The intensities are provided as a function of the wavelength at which the code is working. In this way the simulated PSFs are related with a specific resolution element of the spectrum.

Moreover, every PSF produced in this way is strictly monochromatic. In reality the resolution is very low and the spectral resolution elements are quite large (with  $R=15$  in the near-infrared we expect a  $\Delta\lambda \sim 0.04\mu\text{m}$ ). We solved this problem in a statistical way exploiting the fact that the typical lifetime of a phase screen is a fraction of a millisecond, while a simulated exposure time is usually much larger than 1s. We then calculated the PSF not only at the wavelength  $\lambda$ , center of the resolution element, but also at  $\lambda \pm \lambda_r$ , where  $\lambda_r \leq \Delta\lambda/2$  is a small random value. With this procedure we have enough different values of  $\lambda_r$  to sample all the element uniformly. For this reason, we see an elongation of speckles due to their chromaticity even in an image nominally related to a single wavelength (see Fig.3). We also note that the speckles seem to form a sort of bright ring: this is a characteristic feature of XAO: the central part of the image is better corrected than the external region, and the radius of this “ring” is  $\sim \lambda/2d$  where  $d$  is the interactuator distance

of the wavefront sensor. This radius is also called the Control Radius and is  $\sim 0''.5$  at the shortest wavelength ( $0.95\mu\text{m}$ ) in this application.

The PSF simulated in this way has been compared with real observed data obtained with NACO-SDI at VLT, adapting the input parameters for this specific case. The results showed a good correspondence between the simulated speckle noise and the measured noise, and give confidence in the simulation (Berton et al. 2004).

#### 4.3. The Integral Field Unit and the disperser

The simulated IFU is a microlens array composed of  $254 \times 254$  hexagonal lenses. For the 8 meter telescope, we used a spatial sampling of  $0''.014$  per lens, covering a total field of view of  $3''.5 \times 3''.5$ . To avoid stray light from the gaps between the lenses, we applied a circular mask to every lens. This mask has the disadvantage of blocking in the simulated case the 9.2% of light, but its presence is important to avoid stray light at the edges of the lens. The simulated case is also the best case geometrically possible: the radius of the circular mask  $r_m$  is supposed to be equal to the distance between the center of the hexagon and one of its sides. Mathematically it means that  $r_m = (l/4)\sqrt{3}$ , where  $l$  is the diagonal of the hexagon. This loss of photons has some consequences on the procedure of speckle subtraction, that have to be studied in detail, even if it is considered in the code.

Each microlens of the IFU array samples a small portion of the PSF, and creates its own small PSF which is imaged onto the detector by the IFS optics<sup>5</sup>. The location of these PSFs depends on the geometry chosen for the array and on the size of the lenslets. In CHEOPS IFS the optical design has been optimized to keep the cross talk between the

---

<sup>5</sup> After the microlens array the diffraction of the lenslets is dominant: for this reason, we don't have micropupils on the detector but diffraction limited PSFs

lenses below  $10^{-4}$ , in order to be negligible.

The code considers each lens separately, applying a standard PSF given by the diffraction pattern of a uniformly illuminated circular aperture:

$$i(\theta) = i(0) \left[ \frac{2J_1(v(\theta))}{v(\theta)} \right]^2, \quad (5)$$

where  $\theta$  is the distance from the center,  $J_1$  indicates the Bessel function at 1<sup>st</sup> order and  $v(\theta) = 2\pi\theta/(\lambda F)$  with  $F$  being the focal ratio (in our specific case we used  $F=8$ ).

The next step is the simulation of the disperser. Since the images we simulated up to now (stellar PSF and microlenses) are related to a single resolution element of the spectrum, thus almost monochromatic, we need to repeat the entire procedure in order to simulate all the different wavelengths of the considered spectrum. Every modification in wavelength causes two effects on the speckles on the AO focal plane: a radial shift with respect to the stellar center and a change of the size of both the diffraction figures and the speckles. Moreover, the PSFs of the microlenses will also change. In addition, the fluxes of the star and of the planets must change with wavelength according to their spectra. Final images after the simulation of the IFU for all different wavelengths must then be combined on the detector in order to obtain the observed spectra, shifting the micro-PSF images slightly in a way proportional to their wavelength.

Finally, before concluding the procedure, all noise sources related to the detector are added to the image. These noise sources include read out noise, dark current, flat field etc. The contributions to noise are computed considering the values appropriate for the main near-infrared detector available at present. The used values for the various parameters characterizing the detector are summarized in Tab.1. An example of the output of the whole simulation is presented in Fig.4.

#### 4.4. Data reduction

Fig.4 clearly shows that the spectra in the final image are not as regular as expected from the model of the stellar spectrum shown in Fig.2. The dependence of fluxes on wavelength apparently follows a pseudo-sinusoidal law. This is due to the shift of speckles from one microlens to another with changing wavelength. This effect makes it impossible to do a simple comparison of the spectra for detecting the planet. For this reason, following the example of Sparks & Ford (2002), we must extract all data related to every single resolution element from all the spectra in order to rebuild a set of monochromatic images that can be, at this point, rescaled in size by a factor equal to  $\lambda_0/\lambda$ . Scaling all the monochromatic images at a specific  $\lambda_0$  makes the speckles coincide in position and size, so that a subtraction becomes possible. An example of rebuilt monochromatic image is shown in Fig.5.

The algorithm for subtraction can be different depending on the nature of the planet. In this first analysis, we decided to follow the idea of double-difference presented by Marois et al. (2000), using three images  $I_1$ ,  $I_2$  and  $I_3$  obtained by three resolution elements  $\lambda_1$ ,  $\lambda_2$  and  $\lambda_3$ :

$$D = (I_1 - I_2) - k(I_1 - I_3), \quad (6)$$

where  $k$  is a constant factor depending on the Strehl ratio achievable at the different wavelengths considered:

$$k = \frac{S_1 - S_2}{S_1 - S_3}. \quad (7)$$

With a number of wavelengths available larger than 3, we could apply Eq.6 to various combinations of images, investigating different spectral features and using the entire

information given by the spectra, as explained in Sec.6.1.

An example of detection of a brown dwarf of  $30 M_J$ , 5 Gyr old, orbiting around a solar-type star, is shown in Fig.6. As mentioned above, the mechanism for reduction of speckle noise presented here is useful only if the monochromatic images obtained from the spectra are scaled in an appropriate way: no rescaling (at left) usually makes the companion not detectable, while with a good rescaling procedure (at right) the companion is clearly visible with quite a high signal-to-noise ratio ( $\sim 30$ ).

#### 4.5. Simulation code – Next steps

The CSP code, although it takes into account a large number of parameters and noise sources in order to simulate real observations, can still be improved. Some particulars have been neglected or underestimated for various reasons, sometimes because going too much into details was not the purpose of the work presented here (e.g. the AO system structure), and sometimes because we were interested in immediate performances estimates while a more accurate study would have required excessive computer time. This study will be anyway investigated in detail later.

In particular, the procedure for simulating the microlens array presents some simplifications, and a possible improvement is under study now. At present, this procedure supposes all the lenses to be identical and it associates a standard perfect PSF to each lens, but in reality the phase screen over the entrance pupil of a microlens is not constant. A first set of tests and simulations showed that with our specific choices of focal ratios and spatial sampling, for low static aberrations, the differences between the real observed PSFs of the microlenses and the simulated perfect ones can be neglected for long exposure times, when the speckles are homogenized to form a smooth seeing disk. A study of these differences in

the case of significant static aberrations is ongoing.

Another phenomenon that is currently not well accounted for, is the interference between the microlenses. This interference could modify the shape of the PSFs, making them sometimes too faint to obtain a clear spectrum. An accurate simulation of this effect is very expensive in terms of computer resources, and had to be neglected in this first version of the code. However this is currently being studied in order to determine whether omitting this effect is significant when achieving accurate detections. The results of these studies will be published in the near future.

To be included in our simulations, and consequently in the procedure of analysis of spectra, is a calibration error due to the fact that in the real observations the central wavelength related to every spectral pixels of each spectrum cannot be perfectly known but requires a calibration; in our code this error is probably underestimated, and new studies are ongoing now to understand its importance in the final signal-to-noise ratio of the detections.

Concerning the flat field, one should note that the whole process of generating noise is not simulated in detail. We simply calculated a residual noise of  $10^{-4}$ , as explained in Sec.5.4. A complete analysis of the flat field process could be important for understanding their effect on the final signal-to-noise ratio achievable.

Finally, during or between the real observations we will need to apply some rotations to the field of view. An estimate of the level of noise introduced by these rotations and the following corrections could well be interesting. Moreover, anisoplanatism can also introduce some reductions to the Strehl Ratio of the planet that should be not very significant but have to be studied in detail.

## 5. Results

### 5.1. Compilation of results

Here we present the results of the simulations we made in the case of an observation of various Jupiter-like planets and low-mass brown dwarfs with an 8m-class telescope. For each case we calculated a signal-to-noise ratio, in order to define which kinds of planets are detectable with a signal-to-noise ratio larger than 5, the threshold of detectability. We simulated the following specific cases:

- 4 different planetary masses:  $1, 5, 15, 30 M_J$ .
- 3 values of ages: 0.01, 1, 5 Gyr.
- 3 distances from the Sun: 3, 10, 40 pc.
- 2 types of stars: a G0V and a M0V.
- 3 different seeing conditions: 0.60 (good), 0.85 (median), 1.00 (not so good) arcseconds.
- Various angular separations between the host star and the companion, over a range between  $\sim 0.3$  and  $\sim 2$  arcseconds.

The exposure time was always assumed to be 4 hours.

In this list of cases we found objects warm enough to be characterized only by intrinsic thermal emission, and at the same time old and small planets that shine only due to reflected light. Moreover, usually the planetary spectra are different as a function of the physical separation between planet and star. Thus, the sample we covered is appropriate for a wide group of targets within the capabilities of an 8-meter telescope. We needed a large set of spectral models, that were taken from Burrows et al. (2004).

The main results of the simulations are presented in this section. As secondary results, we also discuss the general capabilities of this technique in removing speckle noise (Sec.5.2), and the frequency of false alarms (Sec.5.3).

In Tab.3 we compiled the signal-to-noise ratios for all the cases listed above, for good seeing conditions (seeing of  $0''.6$ ). The values are expressed as a function of the angular separation from the host star. It is important to note that we tried to be conservative in choosing the various parameters, in order to present a lower limit of the expected signal-to-noise ratios.

For some significant cases we also show plots (Fig.7, left) with the level of noise before and after the subtraction of speckles, the photon noise and the expected signal from the planet. Plots of the measured signal-to-noise ratios versus separations are also shown (Fig.7, right).

Because of the expensive calculations to simulate observations of 4 hours with our code, some of these results have been obtained using scaling laws and a faster spreadsheet which computes the signal-to-noise of a planet image at different separations from the star as expected at the output of a simultaneous differential imager like the one we simulated. This spreadsheet, called CSS (CHEOPS Simulation Spreadsheet) is based both on theoretical estimates and on the simulated PSFs and noises. Many cases presented in Tab.3 have been obtained using both the simulation code and the spreadsheet: the good coincidence of the results allowed us to use it for the detections not easy to simulate: for instance, the objects at angular separation of  $4''.21$  which cannot be simulated because it is out of our field of view. A description of the CSS spreadsheet is presented in Appendix B.

## 5.2. Determination of the factor of reduction of speckle noise

A crucial result of these simulations is the determination of a value characterizing the effective reduction of speckle noise achieved using the SDI technique as suggested in this paper. We know from theory the behaviour of speckle noise as a function of time, flux and Strehl ratio (Eq.2). Applying SDI to the obtained data reduces the noise by a certain factor which we call  $\varepsilon$ . The expression for the reduced speckle noise  $N$  would be this:

$$N = N_{sp}\varepsilon = \sqrt{1.7\pi\frac{\tau_0}{t}} \left[ \left(\frac{\lambda}{D}\right)^2 (1 - S) F_* f_{halo}(\theta) \right] \varepsilon(\theta), \quad (8)$$

where  $N_{sp}$  is the original level of speckle noise and the other variables are as explained in Sec.2. In order to calculate  $\varepsilon$ , we considered first one of the monochromatic images, before the SDI procedure, scaled to the wavelength  $\lambda_0$  of the original image. In this image we analyzed the level of noise  $N_{sp}$  in a set of small regions placed in a radial sector, at different angular separation from the central peak. This radial sector has been chosen to avoid spiders, artifacts and also the simulated planets. We repeated the procedure using the image resulting from the SDI, obtaining a resulting noise  $N_d$ . While in  $N_{sp}$  the speckle noise is strongly dominating, in  $N_d$  the contributions of photon noise  $N_{ph}$  and of other background noise sources ( $B$ , that are detector noise, background sky, etc.) become important. These contributions can be easily derived from the average intensity in the regions analyzed before subtracting for  $N_{ph}$ , and by measuring the level of noise in a peripheral region not affected by speckles.

The formula we used to calculate  $\varepsilon$  is finally, for each portion:

$$\varepsilon(\theta) = \sqrt{\frac{N_d^2(\theta) - N_{ph}^2(\theta) - B^2}{N_{sp}^2(\theta)}}. \quad (9)$$

The quantity  $\theta$  indicates the distance between the center and the different region of the

image. Since the regions are chosen on a radial sector at different separations from the center,  $\theta$  is expressed in arcseconds. We repeated the procedure for different sizes of the regions and for different radial sectors. The results obtained are sometimes quite different because the simulated PSF is not perfectly symmetric. They were averaged in a final  $\varepsilon(\theta)$ .

From Fig.8 we can easily see that the final noise using this technique becomes comparable with the photon noise for the three cases considered (M0V star at 10 pc, G0V star at 10 pc, G0V star at 3 pc). The factor of reduction changes with the separation, but it is  $\sim 10^{-3}$  between  $0''.3$  and  $1''.0$ . This value for  $\varepsilon$  is an indicator of a good suppression of speckle noise.

This result shows that using the SDI technique is actually possible to reach a level of noise comparable with the photon noise. Similar conclusions, in terms of dual band imaging SDI, have been achieved for NACO-SDI in Biller et al. (2006a).

### 5.3. False alarm frequency

We estimated the probability of detecting a false signal with a signal-to-noise ratio between 1 and 7, with a sampling aperture corresponding to  $\sim 2 \times 2$  spatial resolution elements. Using this probability, we could extrapolate the expected number of events in the final differential image. The results are presented in Tab.2. These probabilities clearly demonstrate that the threshold signal-to-noise of 5 is high enough to avoid false alarms. Therefore, we choose this value in an evaluation of detecting planets with the IFS. Moreover, a more confident confirmation of detections can be done repeating the observations under the same conditions if possible, and at different angles. Comparing the position of the detected candidates, we can easily confirm or not if it is a false alarm.

In the case of a large number of observations the number of false alarms can become

more important. With a S/N of 5, we expected one false alarm within 30 observations. This means that a “detection” always has to be checked by additional observations.

#### 5.4. Flat field errors and thermal background

Flat field errors were included as multiplicative terms to the total number of photons detected by each pixel of the detector. Accurate flat fielding is foreseen and images will be obtained using a dithering procedure that spread the signal of the planet over a large number of pixels by allowing the field to rotate from one exposure to the following one (typically, a few thousands of exposures are summed up to provide the total exposure). Therefore it is reasonable to assume that the residual flat field error in a detector pixel can vary between  $10^{-3}$  that can be achieved using an accurate dithering procedure, and the goal of  $10^{-4}$ . This value is assumed in our computations, although it is certainly not easy to achieve. Flat field errors are important for bright sources and for the regions closer to the stars, limiting sometimes the possibility of observing planets by reflected light when using the SDI-IFS. Fig.9 shows this comparison in terms of measured signal-to-noise ratios for a  $15 M_J$  object orbiting a G0V star at 1 Gyr age at 10 pc from the Sun: the detections within 0.3 and 0.6 arcseconds, which was possible without considering flat field errors, are shifted below the threshold of S/N=5.

Concerning the thermal background, which is also a source of errors, we assume that cold edge filters are placed in front of the IFS detectors. These edge filters will reduce the thermal background flux by a factor between  $10^{-4}$  down to  $10^{-5}$ . We adopted this last value in our computations. The thermal background flux is not a serious concern in the  $J$ –band but it may be of some importance for the faintest sources in the  $H$ –band.

### 5.5. Dependence of detection quality on seeing conditions

To show the effect of median ( $0''.85$ ) or relatively bad ( $1''.00$ ) seeing conditions in comparison with the good case described above, we repeated the simulations for a few specific planets, selected in order to avoid too bright or too faint planets. From these simulations it becomes obvious how important it is to work with the best atmospheric conditions when using our method to detect planets.

We show here the results for four significant cases:

- A  $5 M_J$  planet, 1 Gyr old, around a G0V star at 3 pc.
- A  $5 M_J$  one, 1 Gyr old, around a G0V star at 10 pc.
- A  $5 M_J$  one, 1 Gyr old, around a M0V star at 10 pc.
- A  $1 M_J$  one, 0.01 Gyr old, around a M0V star at 40 pc.

The resulting signal-to-noise ratios are presented graphically in Fig.10. The plots show that the quality of detection decreases as the FWHM increases. This is due to the fact that the Strehl Ratio ( $S$ ) achievable by the AO system is different in the three observing conditions. While the achievable signal-to-noise ratio does not change too much when going from optimal (seeing  $0''.60$ , Strehl ratio of 0.80) to good (seeing  $0''.85$ , Strehl ratio of 0.75) conditions, planet detection is clearly much more difficult in the not-so-good condition (seeing  $1''.00$ , Strehl ratio of 0.40)<sup>6</sup>.

---

<sup>6</sup>As explained in Sec.4.1, our AO simulator is not detailed enough to claim a true significance of the dependance of signal-to-noise ratio on seeing. Rather, the Strehl numbers themselves should be seen as independent parameters.

In Fig.11 the signal-to-noise ratio is presented as a function of Strehl ratio for two angular separations. The signal to noise ratios, going from  $S=0.80$  to  $S=0.75$  and  $S=0.40$ , are reduced by a factor of  $\sim 2$ . Since the value of  $S$  depends not only on the atmospheric turbulence and seeing but also on the performances of the AO systems, these plots show in a more general way how important is to work both with a good seeing and with a very efficient AO to detect extrasolar planets.

## 6. Discussion

From the data shown in Tab.3 we can see that most of the targets we simulated to observe are actually detectable. In particular, it is clear that very massive objects ( $30 M_J$ ) and very young ones (0.01 Gyr) are detected at every considered distance with very high signal-to-noise ratios (usually higher than 1 000). In the other cases, the signal-to-noise ratios are strongly dependent on the age and on the mass of the planet, as shown in Fig.12. From these plots we can conclude that the detection is easier in the case of larger masses, or, if the mass is fixed, for young objects.

The less massive objects (from 1 to  $5 M_J$ ) are more interesting targets, but they are also much more difficult to detect. Their potential detection is more sensitive to the distance of the planetary system (they are almost unobservable at 40 pc) because of their faintness in the near-infrared region. In some cases they are shining by reflected light, namely the  $1 M_J$  planets older than 1 Gyr, but also the  $5 M_J$  5 Gyr old. Systems with planets shining by reflected light are the most interesting cases, because of the similarities with the Solar System. Detection of a planet like Jupiter ( $1 M_J$ , 5 Gyr old) around a star almost like the Sun, at a separation around 5 AU, means to observe something so similar to our system to allow us to suppose the presence of terrestrial planets in inner orbits, perhaps even in the habitable zone. All reflected light cases simulated are not detectable with 4 hours of

exposure time, even if they were only at a distance of 3 pc from the Sun. This kind of object is still a challenging goal for such an instrument, at least if it is mounted on an 8m-class telescope. They can be better detected using different strategies dedicated to reflected light, for example the CHEOPS project with the polarization analyzer ZIMPOL.

From the plots in Fig.12 we can also conclude that the SDI-IFS technique allows detection of planets of a few Jupiter masses (around 5), with ages of  $\sim 1$  Gyr, within a distance of 10 pc. Passing from 10 to 3 pc we are not enlarging dramatically the range of planets detectable, as shown by the very thin dark-gray region in both plots. Planets of a few Jupiter masses, up to now, have been directly detected only if they are very young, while we can consider a 1 Gyr planet to be reasonably old. The direct detection of such an object would be a very important result in the present contest of searching for extrasolar planets.

Finally, comparing the two plots, we note that around an M star it is possible to detect more objects at a distance larger than 10 pc. At 40 pc in this case we can detect some interesting old planets down to  $\sim 10 M_J$ . The reason of these better detections for an M star are simply related to the better contrast due to the lower brightness of the M star with respect to a G star at the same distance. The spectral differences between the two stars at this resolution are less important than the differences in flux. Less flux means less photon noise and less speckle noise. In the case of less flux, beside an improvement of the signal-to-noise ratio, we have also an increment in importance of the photon noise of the planet, that becomes predominant in case of very bright planets and at large angular separation of the star: this can be seen, for example, in Fig.10, bottom right, when the signal-to-noise ratio is stabilizing at a given level beyond  $\sim 2$  arcseconds.

Although these results showed that many detections are possible, if we calculate the real probability to find planets in the solar neighborhood we have to notice that the list

of observable targets is not very long, because in the considered ranges of distances (3, 10 and 40 pc) there are only few stars that can harbour planets which are at the same time detectable with our IFS-SDI. With data from the Hipparcos catalog, Desidera (2005) considered a sample of more than 650 stars within 20 pc, evaluating spectral types, ages, metallicities and binarity; for realistic but rather conservative assumptions on the period distribution of giant planets extrapolated from the results of RV surveys, it was concluded that the detection of at least 10 giant planets is actually expected. Half of the chance of finding planets is confined to the best  $\sim$ 80 targets, while with more than 200 we have almost no chances of success. Shrinking the distance to  $\sim$ 3 pc, for which we obtained from simulations the better detections, we reduce the probability to negligible values.

It should not be forgotten that all these results and considerations are related to the case of an 8m-class telescope. It is natural to expect very different results for different instrumental parameters. We suppose that the detection of faint planets, specially those shining by reflecting light, would be significantly easier with a larger telescope, in particular one of the new Extremely Large Telescopes (ELTs) on project, which cover a range of diameters between 20 and 100 m. The structural and technical differences between an ELT and a 8m-class telescope are sometimes not easy and immediate to consider (e.g. segmentations, spiders, AO systems, etc.), so we need new sets of specific simulations to quantify the improvement in signal-to-noise ratios passing from an 8 meter telescope to an ELT. These simulations will be presented in a forthcoming paper.

### 6.1. Advantages in using IFS-SDI

The reasons why an SDI system based on an IFS is preferable to a set of filters can be summarized in three crucial points:

- First of all, with a whole spectrum available we are not forced to study only one spectral feature of the planet. If we have two filters, or three, chosen to observe a specific absorption band, we lose all information coming from the other features. With a spectrum we can actually combine the data on and off different absorption bands to increase the signal-to-noise ratio of our detection (if there are other good features).
- Second, the availability of data at many wavelengths can allow the development of various algorithms and specific methods for data reduction to improve the reduction in speckle noise.
- Finally, the most important reason for using IFS is the possibility of not only detecting extrasolar planets, but also characterizing these objects. In fact, the data available after the subtraction of stellar light allow the study of the spectrum of the planet and its main features, which can be very different according to mass, age, temperature etc. This argument is fundamental to understand that our method can be very useful also in observing planets already discovered in other ways.

Another potential advantage of an IFS, with respect to a conventional dual band imager is that one can actually make an all-reflective design up to the point where the image is formed, minimizing chromatic errors (as already said in Sec.4).

We present in this section a test made on the simulated images in order to verify the first two points expressed above, that means the actual gain in signal-to-noise ratio and noise reduction due to analysis of a number of wavelengths larger than 2 or 3. To do this, we applied four different operations to the monochromatic images obtained from the spectra, accurately rescaled to a given wavelength. The four operations combine 2, 3, 6 and 9 different resolution elements. The images are indicated by  $I_n$ .

1. Single difference, with 2 elements:  $I_2 - I_1$ .

2. Double difference, with 3 elements, which is Eq.6.

3.  $3^{rd}$  difference, with 6 elements, is given by

$$\begin{aligned} DDD = & [(I_1 - I_2) - k_1 (I_1 - I_3)] + \\ & - K [(I_4 - I_5) - k_2 (I_4 - I_6)] . \end{aligned} \quad (10)$$

4. The  $4^{th}$  difference is a combination of two  $3^{rd}$  differences:

$$\begin{aligned} DDDD = & DDD_1 - \kappa DDD_2 = \\ & [(I_1 - I_2) - k_1 (I_1 - I_3)] + \\ & - K_1 [(I_4 - I_5) - k_2 (I_4 - I_6)] + \\ & - \kappa [(I_4 - I_5) - k_3 (I_4 - I_6)] + \\ & + \kappa K_2 [(I_7 - I_8) - k_4 (I_7 - I_9)] . \end{aligned} \quad (11)$$

The values  $k_n$ ,  $K_n$  and  $\kappa$  are constants that have to be defined case by case in order to subtract the speckles and their residuals as best as possible. Every subtraction, other than reducing speckle noise, introduces a slight increment of the other sources of noise (photons, sky background, detector noises etc.) that has to be considered carefully.

At first, we measured the total level of noise in a specific region of the stellar PSF normally dominated by speckles (in our case, for an 8m-class telescope, we worked between 0.4 and 0.6 arcseconds, avoiding spiders and artifacts). We used different simulations of the same object, and we obtained averaged values of residual noise in this region using all the four different algorithms. All these calculations of noise have been done without planets. We calculated then the signal of a planet, chosen bright enough to be detectable clearly (signal-to-noise ratio  $\sim 5$ ) with the single difference method, and with all but one of the resolution elements considered in absorption bands: practically, the signal of the planet is significant only in one of the nine cases. In this way, we simulated a detection using nine

different wavelengths but only one of the three “peaks” of the planetary spectrum shown in Fig.1. We calculated the signal-to-noise ratios of the detection, as a function of the operation used for subtracting speckle noise.

In a second step, we tried to elaborate the results a little more in order to also use the other “peaks” of the spectrum of the planet. Practically, considering that the signal of the planet in SDI is given by the contrast in flux of the planet on and off an absorption band, we combined the contrasts in two of the three peaks to increase the signal-to-noise ratio. We used the spectrum of a  $1 M_J$  planet at 1AU from a solar-type star (Fig.1 at bottom), where we have two peaks of very similar maximum intensity. The results are shown in Fig.13.

It appears obvious from this plot that a number of resolution elements larger than 3 can actually improve the signal-to-noise ratio of the detection. In fact the improvement is significant, but not dramatic, because just after the double difference the total noise is less dominated by speckles and more by photons. The photon noise represents a limit that cannot be over passed just combining more elements. Moreover, with 9 resolution elements the signal-to-noise ratio doesn't increase. To conclude, a combination of six elements seems to be the best solution for reducing speckle noise, keeping all the other sources of noise under control.

On the other hand, the simultaneous use of other planetary features, represented by the three “peaks” of Fig.1 at bottom, provides an interesting improvement of the signal of the planet, and consequently of the signal-to-noise ratio. Actually, we used only the two highest peaks at  $\sim 1.25$  and  $\sim 1.60 \mu\text{m}$ , because the contribution of the third peak (at  $\sim 1.05 \mu\text{m}$ ) is negligible if compared with the increment of noise combining it with the other data. As shown in Fig.13, we actually improved the signal-to-noise ratio by a factor of  $\sim \sqrt{2}$ , because the contrast for both peaks is very similar. Since a dual band imager can enhance some specific spectral features depending on the used filters, it is not easily achievable to observe

at the same time many of these different features, while to have all the peaks in a single simultaneous exposure is possible with IFS.

## 7. Conclusion

With numerical simulations we evaluated the capabilities of an IFS instrument to reduce speckle noise. One can achieve a reduction factor of  $10^{-3}$ , which can be considered a good result for the SDI technique. It allows the detection of a vast range of faint companions around stars in the solar neighbourhood. For an 8m-class telescope, our simulations have shown that objects of a few Jupiter masses can be clearly detected within 10 pc, with very high signal-to-noise for the most massive and youngest ones. Much more difficult will be the detection of old and cold Jupiter-like planets shining by reflected light. From these first simulations it seems that such an instrument mounted on an 8 meter telescope cannot detect planets like Jupiter in a system like our Solar System, at least with exposures of 4 hours or shorter. Despite this the IFS method has some very important advantages that should not be neglected, in particular the possibility to characterize the planet by studying its spectrum. This IFS-SDI is not only useful for planet detection, but in cases of relatively high signal-to-noise ratio we can extract its whole near-infrared low resolution spectrum. This characterization is not completely possible in narrow band SDI systems working with only two or three defined filters, while it becomes possible for SDI-IFS because of the large spectral information available. This technique appears to be extremely useful, if not for detecting very cold and small objects, for a better detection and characterization of planets younger than 1 Gyr or more massive than a few Jupiter masses. The structure of the simulation code, which is versatile and adaptable to different kinds of instruments, will also allow simulation of telescopes larger than 8 meters (ELTs). We expected to have a significant improvement of the quality of detection in case of diameters

of 20, 50 or 100m; and we expect, in that case, that also young and cold planets can be detectable with short exposure times: this will be the topic of a forthcoming paper.

This work started during the phase A of the CHEOPS project for a Planet Finder instrument at VLT on Cerro Paranal (Chile). It was supported by the European Southern Observatory (ESO). The authors wish to thank all the people involved in the CHEOPS project for the useful collaboration during this phase A. A. Berton wants to thank Kjetil Dohlen from the Laboratoire d’Astrophysique de Marseille for his important suggestions and comments, and Catherine Heymans from the University of British Columbia, Vancouver, for her kind help.

### A. Flux contrasts for the considered cases

In Tab.4 and in Fig.14 and Fig.15 we report an analysis of the flux contrasts between the intensity peaks of the planets and stars considered in Sec.5, calculated in  $J$  band. In the four plots of Fig.14 these contrasts have been represented as a function of the angular separation, always expressed in arcseconds. The contrast are also plotted with respect to the mass of the planet and to the age of the system. The contrast are calculated for a distance of 3 pc from the Sun; moreover, in both Fig.14 and Fig.15, at bottom right, the contrasts for a  $1 M_J$  and 1 Gyr old planet at different distances are presented. The magnitudes of the planets in  $J$  band are taken from Baraffe et al. (2003), and the fluxes at various separations are computed used the CSS spreadsheet described in Appendix B.

From the plots we can see the different behaviour of the contrast of reflecting planets, if compared to thermally emitting planets: the formers present a decrement in flux at large separation, due to the dependance of the flux on the distance  $d^{-2}$  (Eq.B1); the latters present the same decrement but only very close to the host star, while at larger separations

the reflection of stellar light becomes negligible with respect to the intrinsic emission, and the contrast becomes a constant.

Even if in the plots the main results are presented for a distance of 3 pc, the values of contrast obtained for warm thermally emitting planets are expected to remain the same also at different distances (except for a small region close to the star). For less massive or older planets this is not true, because the flux depends on the physical separation between star and planet, and at a larger distance this separation appears under a smaller angular separation. For this reason, the plots for different distances have been drawn only for planet shining by reflecting light (1  $M_J$ , 1 Gyr old).

Tab.4 summarizes these contrasts for all the studied cases, for planets at a separation of 1 AU from their host star. Since the physical separation is fixed, these results are valid at every distance from the Sun.

## B. CHEOPS Simulation Spreadsheet

CSS calculates a set of signal-to-noise ratios of a monochromatic planet image (assumed to have the size of the Airy disk) at different separations from the star, as expected as output of a simultaneous differential imager like the CHEOPS IFS channel. Adapting the instrumental parameters to various cases, it can be used for IFS instruments other than the specific CHEOPS case. The signal is computed in physical units in different bands ( $R$ ,  $I$ ,  $J$ ,  $H$ ,  $K$ ,  $L'$  and  $M$ -bands) for both the star and the planet. Various choices are possible for the basic parameters: stellar luminosity and distance, various planet ages and masses, planet-star separation, etc. Both intrinsic emission and reflected stellar light are considered. The intrinsic emission from planets is estimated using magnitudes from Baraffe et al. (2003) COND models. Since a flat spectrum is assumed within each band, fluxes at the "emission

peaks” in the  $J$  and  $H$  bands are underestimated by a factor of 2-3. For the reflecting light, it is assumed that the planet is at quadrature, so that the projected physical separation is the real star-planet distance divided by the distance of the star from us; and that only a fraction  $A_\lambda$  of the light is reflected,  $A_\lambda$  being the geometrical albedo from Sudarsky et al. (2000), dependent on wavelength, and has to be multiplied by the phase factor  $\phi$  (0.41 for a specific phase angle of  $80^\circ$ ) to include the geometrical effects:

$$F_{ref} = F_* \frac{\phi A_\lambda R_p^2}{d^2}, \quad (B1)$$

where  $F_{ref}$  is the reflected flux from the planet,  $F_*$  is the stellar flux,  $d$  is the distance between star and planet and  $R_p$  is the planetary radius.

Noise estimates include the contributions of the star and planet photon statistics, sky background, detector, and speckles, this last possibly suppressed by any predefined value. The photon noise  $N_{ph}$  is computed assuming a Poisson distribution. The sky background ( $B$ ) is computed using values appropriate for Paranal, in dark sky conditions. Multiple exposures are explicitly taken into account to estimate the contribution of detector read-out noise ( $RON$ ). Speckle noise is estimated as the photon noise times the square root of the total number of photons per speckle. This is obtained by dividing the number of detected photons (in the selected pass bands) by the number of speckles  $n$ , which can be obtained by Eq.1:

$$N_s = N_{ph} \varepsilon \sqrt{\frac{F_*}{n}}. \quad (B2)$$

The factor of reduction of speckle noise  $\varepsilon$ , that was in Sec.5.2 a function of angular separation, is here an average value for all the separations. Its value, previously calculated to be around  $10^{-3}$ , is here enlarged to  $10^{-2}$  to have more conservative results. The total noise  $N_t$  can be expressed in this way:

$$N_t = \sqrt{N_{ph}^2 + N_s^2 + N_p^2 + B + RON^2} =$$

$$= \sqrt{f_{seeing}(\theta) \left( 1 + \varepsilon^2 \frac{F_*}{n} \right) + f_{diff}(\theta) + F_p + B + RON^2}. \quad (B3)$$

We indicated with  $f_{seeing}$  and  $f_{diff}$  the different contribution given to the total flux by the stellar halo and core, this one being a diffraction-limited PSF.  $N_p$ , the noise due to the planetary flux, is expressed as the square root of the flux coming from the planet,  $F_p$ , which is the sum of both reflected and intrinsic emission.

Various instrumental parameters can be defined, including spectral bandwidth, instrument efficiency, adaptive optics Strehl ratio, stray light level, etc. Various options are also possible for the atmospheric conditions (represented by the coherence time  $\tau$ , usually adopted to be 3 ms in this paper, and by the seeing FWHM). The seeing PSF is assumed to be of the form defined by Racine et al. (1999). The diffraction PSF is given by a power law (with exponent  $-2.8$ ), which fits well the PSF produced by detailed simulations.

## REFERENCES

Baba, N., & Murakami, N. 2003, PASP, 115, 1363

Bacon, R., Copin, Y., Monnet, G., et al. 2001, MNRAS, 326, 23

Baraffe, I., Chabrier, G., Barman, T. S., Allard, F., & Hauschildt, P. H. 2003, A&A, 402, 701

Beichman, C. A., Woolf, N. J., & Lindensmith, C. A. 1999, JPL Publications, 99, 3

Bertone, A., Kellner, S., Feldt, M., et al. 2004, in *Advancements in Adaptive Optics*. Edited by Domenico B. Calia, Brent L. Ellerbroek, and Roberto Ragazzoni. *Proceedings of the SPIE*, Volume 5490, 661-671

Bracewell, R. N. 1978, Nature, 274, 780

Biller, B. A., Close, L. M., Lenzen R., et al. 2006, *astro-ph/0601059*

Biller, B. A., Close, L. M., Masciadri, E., et al. 2006, *astro-ph/0601062*

Biller, B. A., Kasper, M., Close, L. M., et al. 2006, *astro-ph/0601440*

Burrows, A., Sudarsky, D., & Lunine, J. I. 2003, ApJ, 596, 587

Burrows, A., Sudarsky, D., & Hubeny, I. 2004, ApJ, 609, 407

Chauvin, G., Lagrange, A. M., Dumas, C., et al. 2004, A&A, 425, L29

Chelli, A. 2005, A&A, 441, 1205

Claudi, R. U., Turatto, M., Gratton, R. G., et al 2004, in *Ground-based Instrumentation for Astronomy*. Edited by Alan F. M. Moorwood and Iye Masanori. *Proceedings of the SPIE*, Volume 5492, 1351-1361

Codona, J. L., & Angel, R. 2004, ApJ, 604, L117

Desidera, S. 2005, in preparation

Feldt, M., Henning, T., Hippler, S., et al. 2005, in Exploring the Cosmic Frontier: Astrophysical Instruments for the 21<sup>st</sup> century, ESO Astrophysics Symposia, Berlin, Germany, in press.

Fridlund, M. 2002, in ESA SP-485: Stellar Structure and Habitable Planet Finding, 235-242

Gisler, D., Schmid, H. M., Thalmann, C., et al. 2004, in Ground-based Instrumentation for Astronomy. Edited by Alan F. M. Moorwood and Iye Masanori. Proceedings of the SPIE, Volume 5492, 463-474

Guyon, O. 2004, ApJ, 615, 562

Labeyrie, A. 2004, in EAS Publication Series, 3-10

Lane, R. G., Glindemann, A., & Dainty, J. C. 1992, Waves in Random Media, 2, 209

Lenzen, R., Close, L., Brandner, W., Biller, B., & Hartung, M. 2004, in Ground-based Instrumentation for Astronomy. Edited by Alan F. M. Moorwood and Iye Masanori. Proceedings of the SPIE, Volume 5492, 970-977

Marois, C., Doyon, R., Racine, R., & Nadeau, D. 2000, PASP, 112, 91

Povel, H. P. 1998, in Astronomische Gesellschaft Meeting Abstracts, 7-+

Racine, R., Walker, G. A. H., Nadeau, D., Doyon, R., & Marois, C. 1999, PASP, 111, 587

Roddier, F., Gilli, J. M., & Lund, G. 1982, Journal of Optics, 13, 263

Rosenthal, E. D., Gurwell, M. A., & Ho, P. T. P. 1996, Nature, 384, 243

Sivaramakrishnan, A., Koresko, C. D., Makidon, R. B., Berkefeld, T., & Kuchner, M. J. 2001, *ApJ*, 552, 397

Sivaramakrishnan, A., Yaitskova, N. 2005, *ApJ*, 626, L65

Smith, W. H. 1987, *PASP*, 99, 1344

Stam, D. M., Hovenier, J. W., & Waters, L. B. F. M. 2004, *A&A*, 428, 663

Sparks, W. B., & Ford, H. C. 2002, *ApJ*, 578, 543

Sudarsky, D., Burrows, A., & Pinto, P. 2000, *ApJ*, 538, 885

Woolf, N., & Angel, J. R. 1998, *ARA&A*, 36, 507

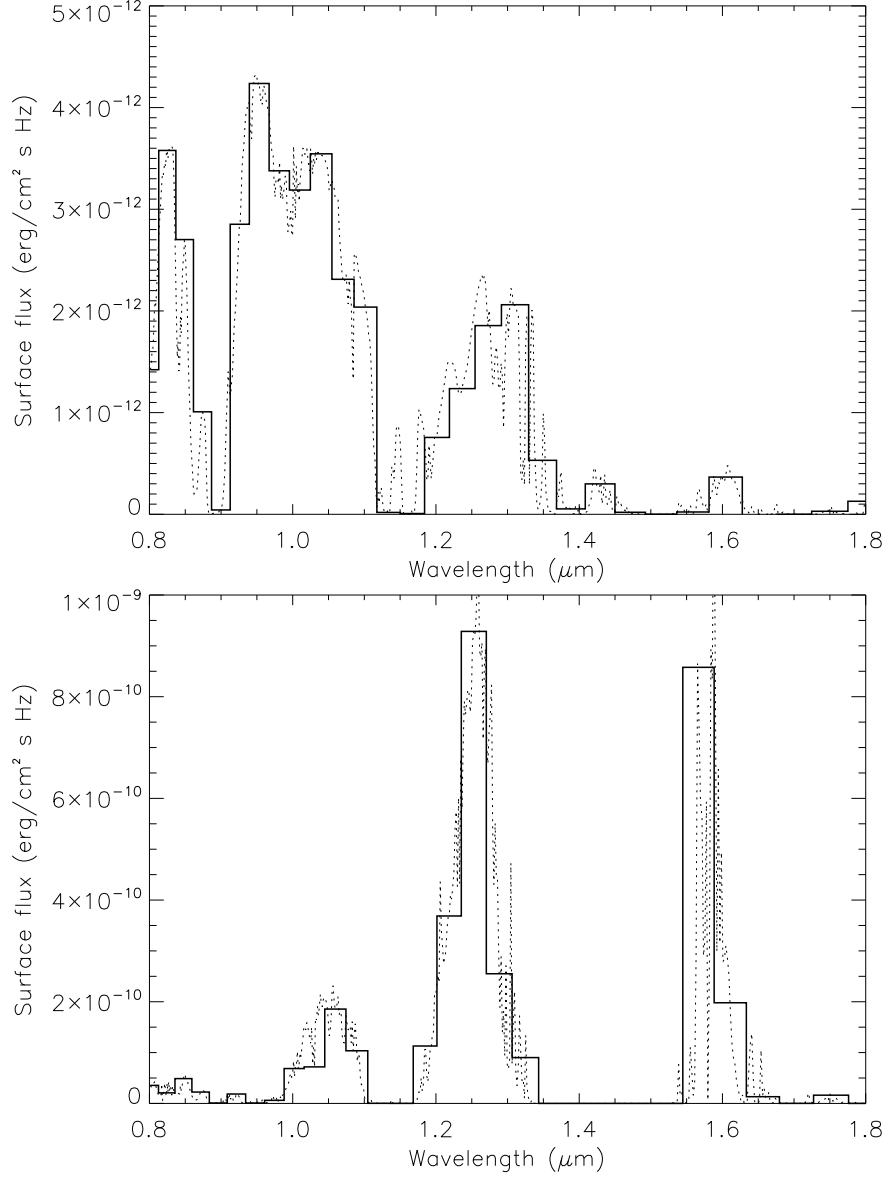


Fig. 1.— Top: Near-infrared spectrum (between  $0.8$  and  $1.8\mu\text{m}$ ) of a  $1\text{M}_J$  planet orbiting a solar-type star (G2V) 1 Gyr old, with a separation of 10 AU. Bottom: The spectrum of the same planet but at a separation of 1AU. For both these planets the spectral emission is mainly intrinsic, with a negligible component of reflected light. The solid spectrum has a spectral resolution of 30, the dotted line of 750. Data taken from Burrows et al. (2004).

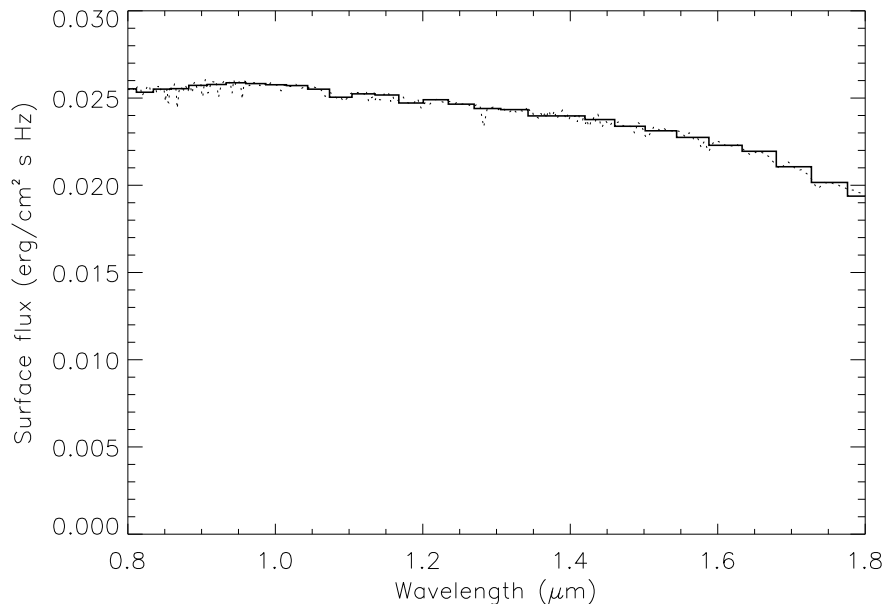


Fig. 2.— Near-Infrared spectrum (between  $0.8$  and  $1.8\mu\text{m}$ ) of a G2V star at the spectral resolution of 30 (solid line) and 750 (dotted line). In this plot are not included the absorptions caused by terrestrial atmosphere. Data taken from Burrows et al. (2004).

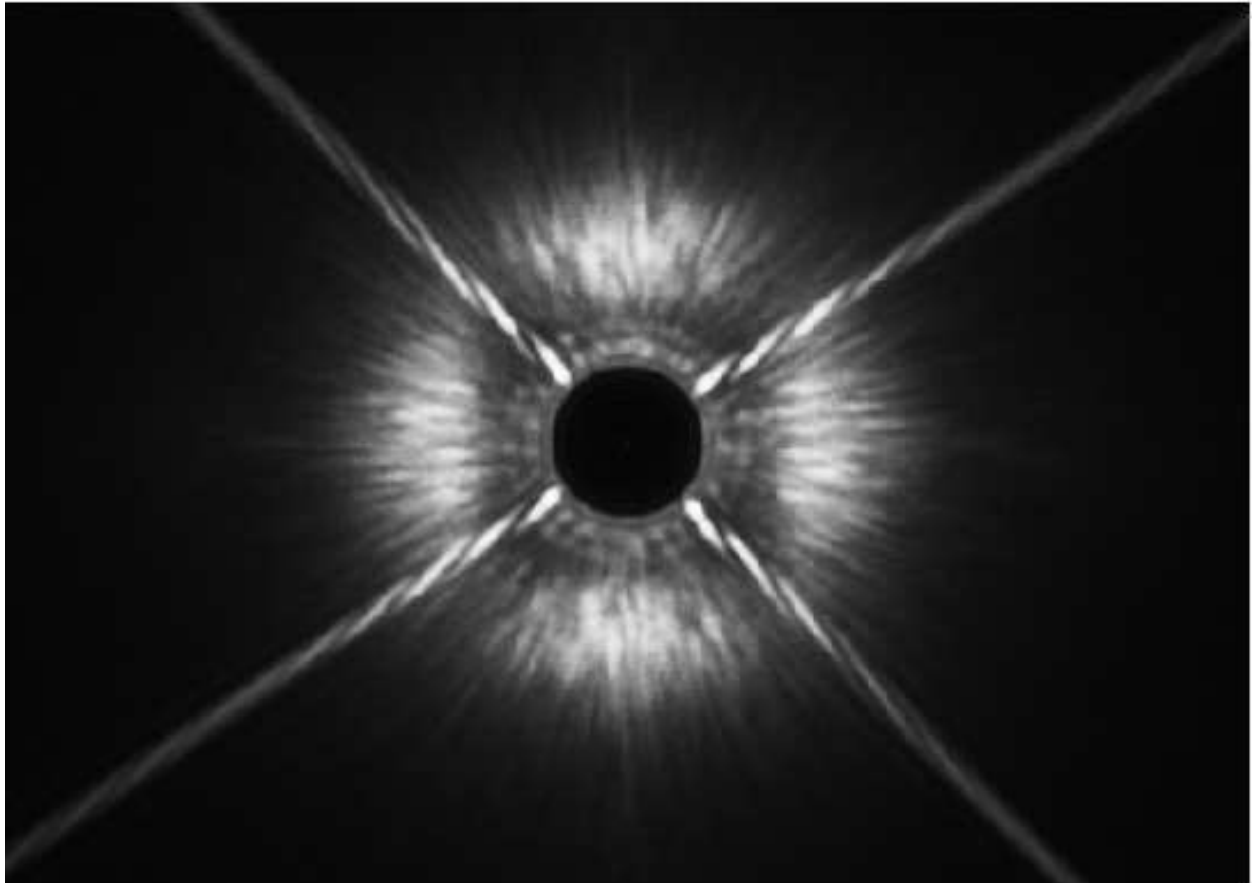


Fig. 3.— Simulated Point Spread Function of a G0 V star at the VLT (prototype of an 8m-class telescope). It corresponds to an integration time of 0.5s, with a Strehl Ratio  $\sim 0.8$  at  $\lambda = 1.0\mu\text{m}$ . The width of the simulated resolution element ( $\Delta\lambda$ ) is  $0.04\mu\text{m}$ . VLT's spiders are clearly visible, as well as the central obscuration with a diameter of  $0''.55$  due to the coronograph.

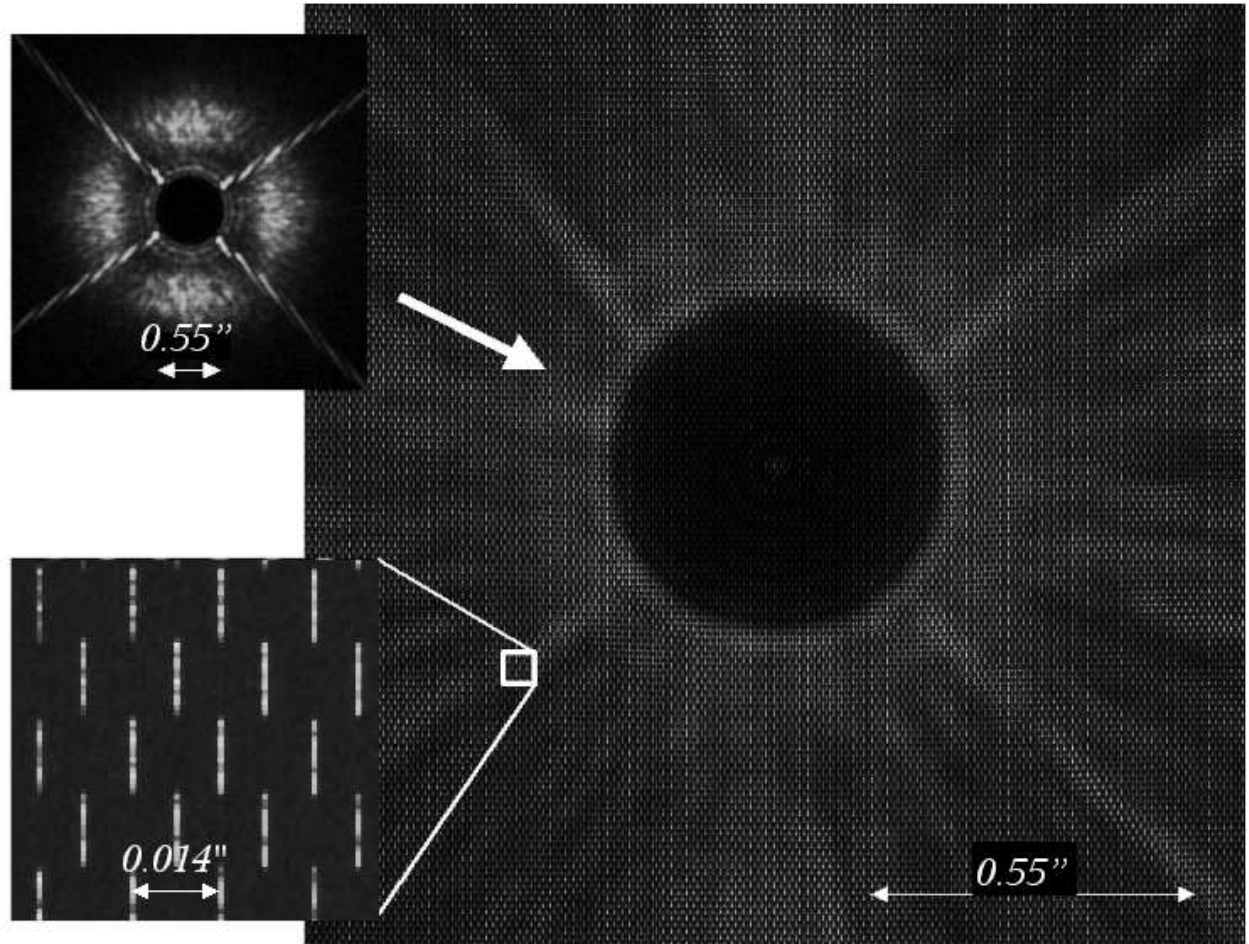


Fig. 4.— Final output of an IFS observation of a star, in the case of the VLT and with the details described in the text. At top left, an example of PSF (with coronographic mask, spiders and AO correction) is presented. After the simulation of IFU and disperser we obtain the large image. At bottom left details of the spectra can be seen. Separations are expressed in arcseconds. The spectra cover the spectral region between 0.95 and  $1.70\mu\text{m}$ , with a resolution of 15, so their spectral length is about 20 pixels.

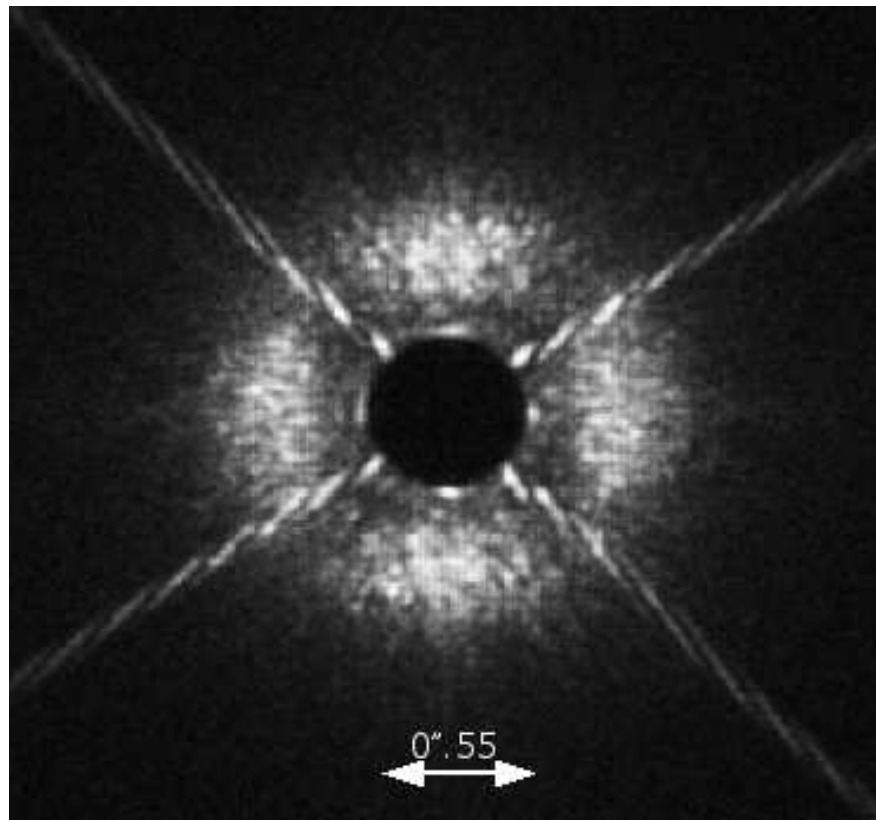


Fig. 5.— A rebuilt monochromatic image obtained by the procedure of data reduction of the simulation code. As explained in the text, from the spectra we obtain a set of images like this that, after a scaling procedure in size, can be compared each other in order to enhance the planetary signal.

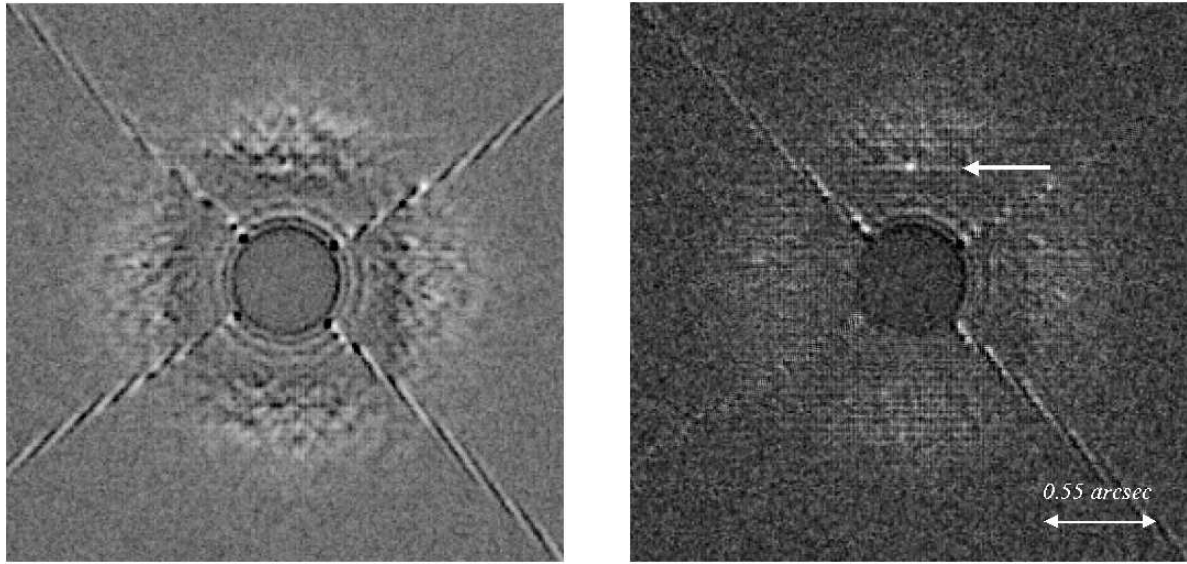


Fig. 6.— Detection of a simulated brown dwarf of  $30 M_J$  after 1 hour of exposure time, around a 5 Gyr old G0V star at 40 pc. Left: three images obtained at different wavelength, on and off a methane absorption band, are combined using Eq.6 but without an accurate spatial scaling: the brown dwarf is visible, but at a signal-to-noise ratio low enough to confuse it with a false alarm. Right: the results of the same operation, but now rescaling appropriately the images by a factor  $\lambda_0/\lambda$  (see Sec.4.4). An appropriate scale factor has been applied also to the fluxes. The result is a clear unambiguous detection of the companion, not possible without application of the rescaling procedure, with a signal-to-noise ratio of  $\sim 30$ .

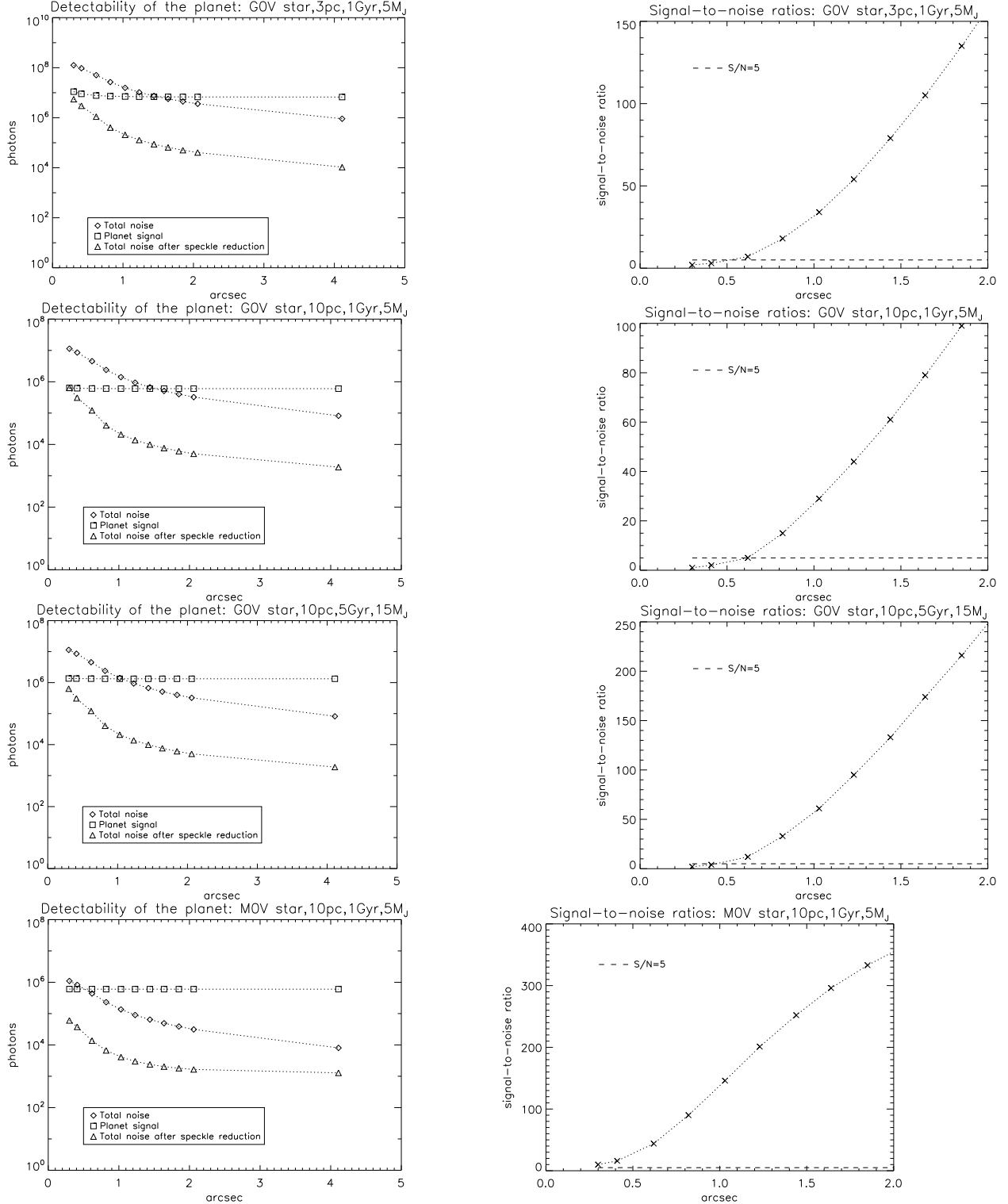


Fig. 7.— Left: The levels of signal and noise are shown, before and after SDI, for four cases. Right: The derived signal-to-noise ratios. The cases are, from top to bottom: G0V star, 3 pc, 1 Gyr, 5 M<sub>J</sub>; G0V star, 10 pc, 1 Gyr, 5 M<sub>J</sub>; G0V star, 10 pc, 5 Gyr, 15 M<sub>J</sub>; M0V star, 10 pc, 1 Gyr, 5 M<sub>J</sub>.

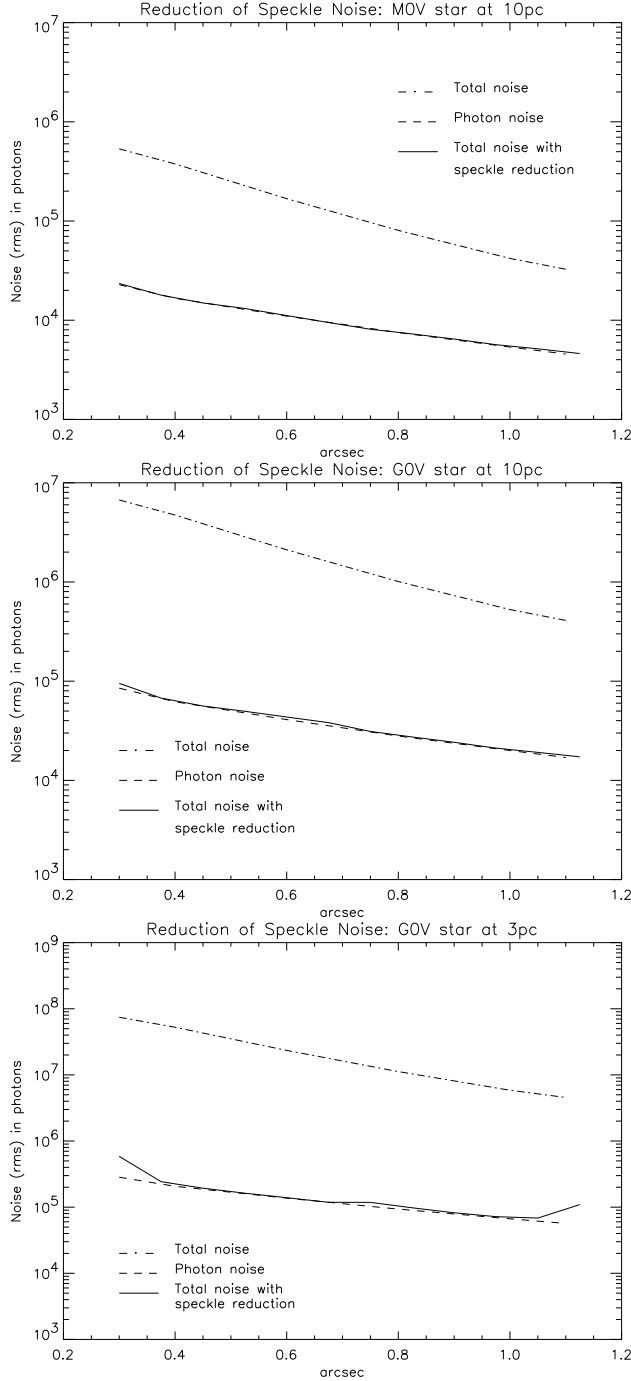


Fig. 8.— Reduction of the speckle noise as a function of the angular separation from the star: Dash dotted line represents the total level of noise before SDI, dominated by speckle noise. The dashed line is the photon noise. The solid line is the total noise after application of SDI. Top: the case of an M0V star at 10pc from the Sun. Center: a G0V star at 10pc. Bottom: a G0V star at 3pc. In all cases we obtained reductions of a factor around  $10^{-3}$ , and the final level of noise is very close to the photon noise.

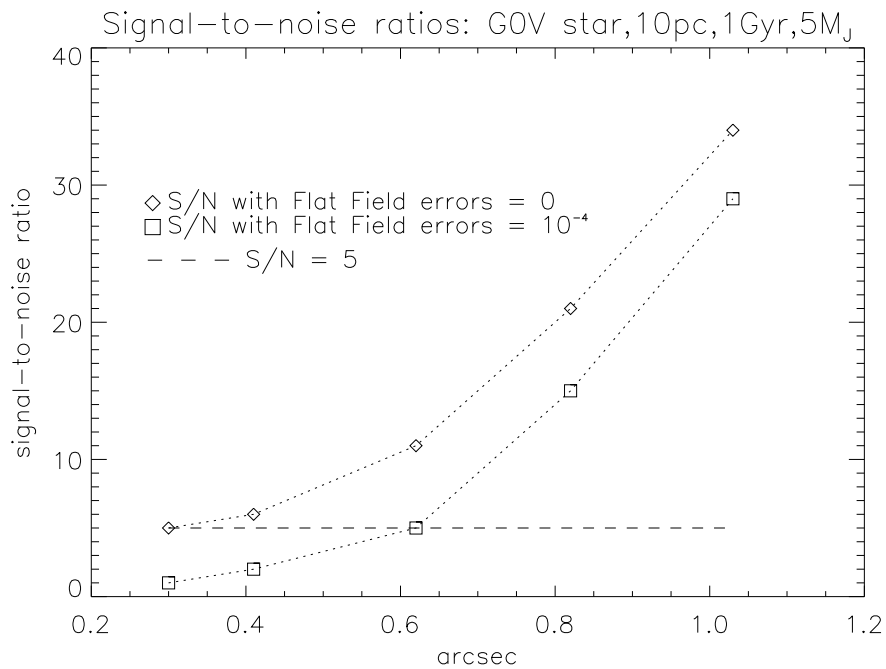


Fig. 9.— Importance of flat field errors in detecting companions. In the case of a  $15 M_J$  object, around a G0V star (age 1 Gyr and at 10 pc from the Sun), the signal-to-noise ratios decrease below 5 (dashed line) in the region closest to the star.

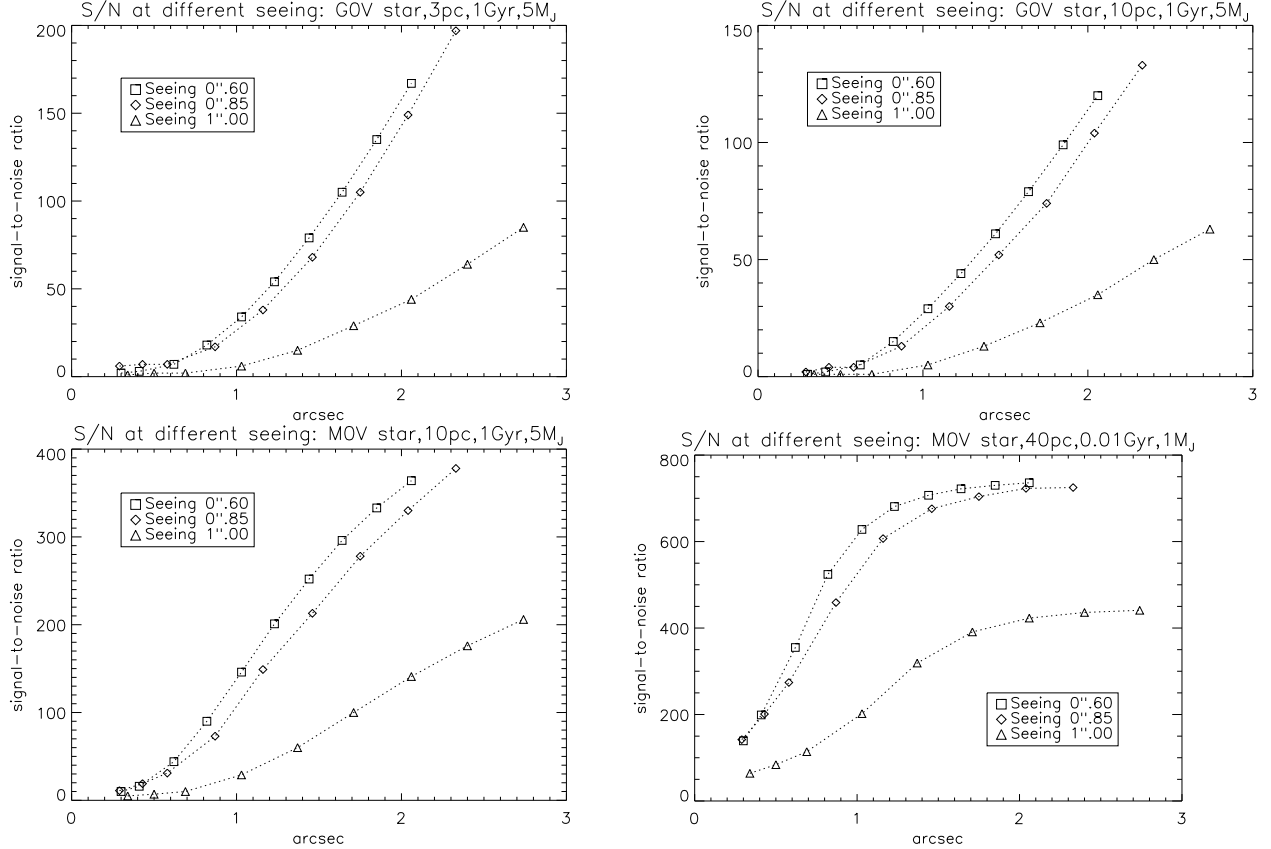


Fig. 10.— Signal-to-noise ratios for detection of four planets at three different seeing conditions and at different angular separations. The four cases are described in Sec.5.5. Every value of seeing have to be associated to a Strehl Ratio  $S$  as explained in the text:  $S=0.80$  for the best seeing ( $0''.60$ ),  $S=0.75$  for the median ( $0''.80$ ) and  $S=0.40$  for the worst case ( $1''.00$ ). While the ratios are quite similar between  $S=0.80$  and  $S=0.75$ , they decrease dramatically in case of a seeing of  $1''.00$ , because of the Strehl ratio achievable by the optical system, which is only 0.40.

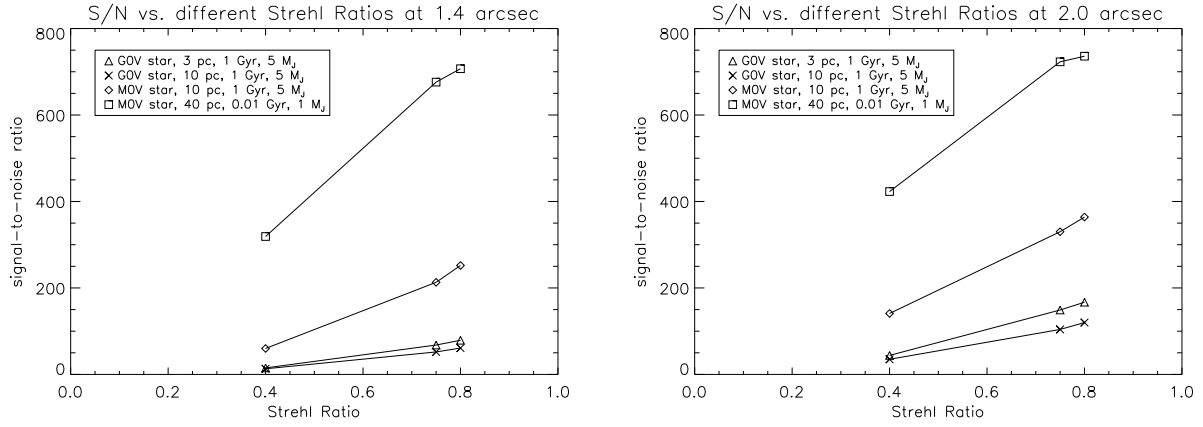


Fig. 11.— Signal-to-noise ratios as a function of the achieved Strehl ratio under the three seeing conditions, measured at 2 angular separations: 1''.4 and 2''.0. The four planets studied are described in Sec.5.5. The Strehl Ratios are strongly dependent on the seeing and on the capabilities of the AO system.

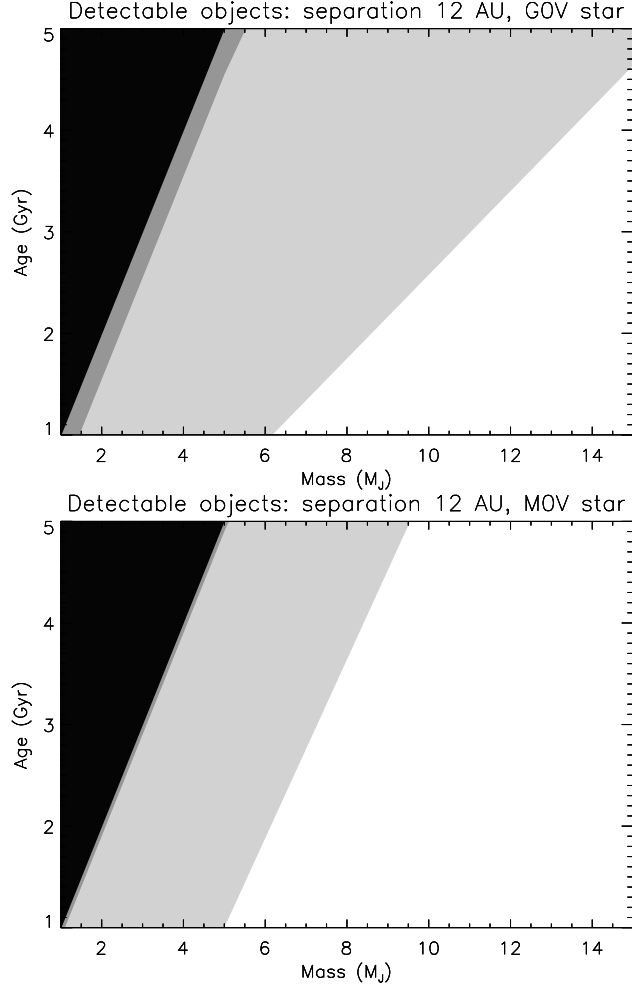


Fig. 12.— Top: planets detectable with a signal-to-noise ratio higher than 5, as function of mass and age, in the case of a G0V host star. The most massive objects ( $30 M_J$ ) and the youngest planets (0.01 Gyr) are not included in the plot because they can always be detected. The white region represents the planets always detectable, for all the distances considered (3, 10 and 40 pc). In the light-gray region there are the planets not detectable if they are at 40 pc from the Sun, but detectable at 10 and 3 pc. In the dark-gray region the planet are not detectable if they are located at 10 pc or further away, but they are visible at 3 pc. In the black region planets are detectable at none of the considered distances. The physical separation between the star and the planet has been kept at 12 AU, but this is changing the angular separations, which are respectively  $4''.0$  at 3 pc,  $1''.2$  at 10 pc and  $0''.3$  at 40 pc. Bottom: the same plot as before calculated for an M0V star. Both these plots have been obtained using data from Tab.3.

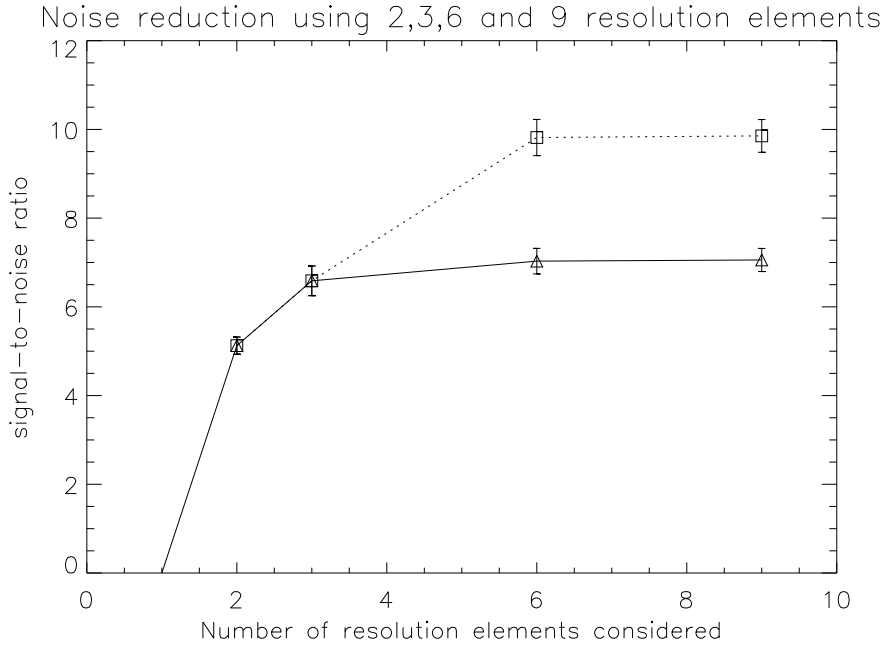


Fig. 13.— Improvement of signal-to-noise ratio of a detection using combinations of different numbers of resolution elements. The triangles connected by the solid line are the results obtained considering a single planetary spectral features; the squares, connected by a dotted line, are obtained considering simultaneously two similar features, which is possible only with IFS-SDI and only considering more than 3 resolution elements. More details are explained in the text. The noise level for this plot has been calculated in various regions of the images and using various simulations of the same object, so the result shown are averaged signal-to-noise ratios with error bars given by the standard deviations. Although the improvement in detection is not very dramatic using only one spectral feature and a number of resolution elements larger than 3, the possibility of using two spectral features instead of one can be really significant, as shown by the dotted line in the plot.

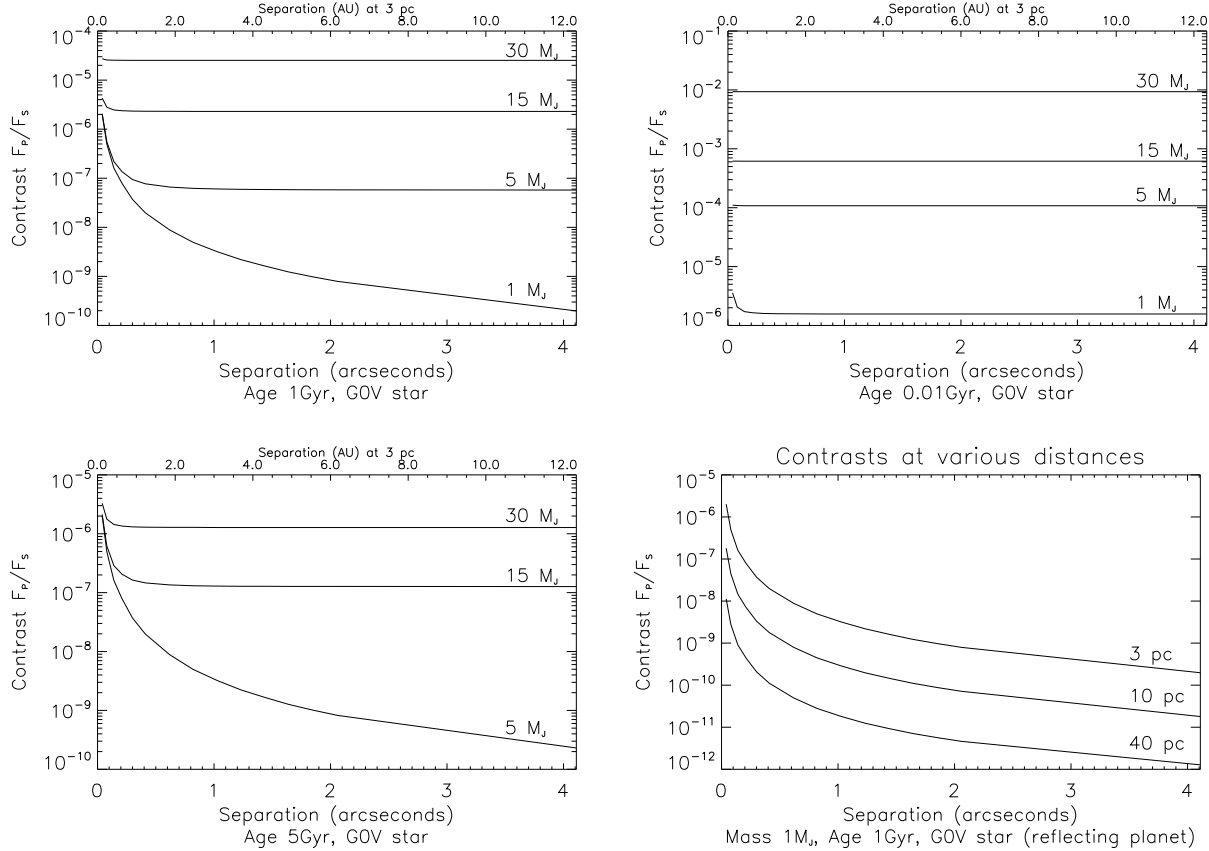


Fig. 14.— Contrasts between the flux of the central peak of a planet ( $F_P$ ) and the flux of the central peak of the host star ( $F_S$ ) as function of the angular separation, calculated in  $J$  band for the planets simulated in Sec.5. The star is always a G0V star and the distance 3 pc, the ages of the system are 1 Gyr (top-left), 10 Myr (top-right) and 5 Gyr (bottom-left). In each plot the results are computed for four different masses (1, 5, 15, 30  $M_J$ ). The physical separation in AU is also reported. At bottom-right: the contrasts as function of the angular separations for a 1  $M_J$ , 1 Gyr old planet in a system at 3, 10 and 40 pc from the Sun. Data taken from Baraffe et al. (2003).

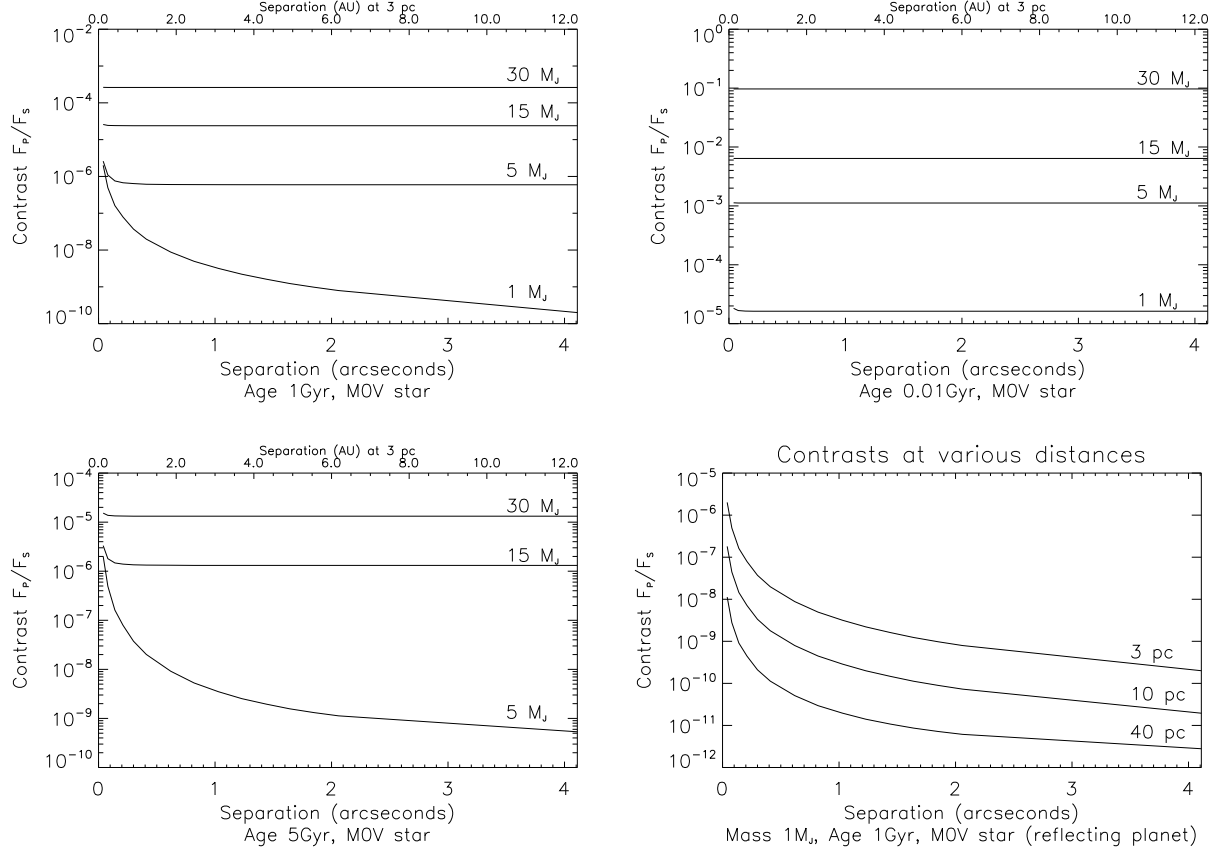


Fig. 15.— Contrasts between the flux of the central peak of a planet ( $F_p$ ) and the flux of the central peak of the host star ( $F_s$ ) as function of the angular separation, calculated in  $J$  band for the planets simulated in Sec.5. These plots are equivalent to the one in Fig.14, but the star is a M0V star. Data taken from Baraffe et al. (2003). See text for details.

Table 1: Main detector parameters introduced in the simulations.

Parameter	Used value
Read out noise	$10 \text{ e}^-$
Gain	$10 \text{ e}^-/\text{ADU}$
Filling factor	0.9
Flat field error	$10^{-4}$ (see Sec.5.4)
Bit resolution	14 bit
Average quantum efficiency	0.6
Dark current	$0.1 \text{ e}^-/\text{s}$
Full well	30 000 ADU

Table 2: Probability of detection of false alarms, and expected number per final differential image.

Signal-to-noise	Probability	Number of events
1	0.3504	1347
2	0.0921	354
3	0.0099	38
4	$4.405 \times 10^{-4}$	1.7
5	$8.007 \times 10^{-6}$	0.031
6	$5.974 \times 10^{-8}$	$2.30 \times 10^{-4}$
7	$1.829 \times 10^{-10}$	$7.03 \times 10^{-7}$

Table 3. Signal-to-noise ratios of the simulated planets and Brown Dwarfs for seeing  $0''.6$ .  $ST$  is the spectral type of the star,  $d$  the distance in parsecs,  $A$  the age in Gyr,  $M$  the mass of the planet in  $M_J$ . The angular separations are expressed in arcseconds. The symbol  $>$  indicates a ratio larger than  $10^3$ , and it means a sure detection.

Angular separations:				0.3	0.41	0.62	0.82	1.03	1.23	1.44	1.64	1.85	2.06	4.21
$ST$	$d$	$A$	$M$											
G0V	3	0.01	1	29	52	163	427	845	>	>	>	>	>	>
G0V	3	0.01	5	>	>	>	>	>	>	>	>	>	>	>
G0V	3	0.01	15	>	>	>	>	>	>	>	>	>	>	>
G0V	3	0.01	30	>	>	>	>	>	>	>	>	>	>	>
G0V	3	1	1	1	1	1	1	2	2	2	2	2	2	2
G0V	3	1	5	2	3	7	18	34	54	79	105	135	167	634
G0V	3	1	15	42	79	268	802	>	>	>	>	>	>	>
G0V	3	1	30	442	812	>	>	>	>	>	>	>	>	>
G0V	3	5	5	1	1	1	1	2	2	2	2	2	2	3
G0V	3	5	15	3	5	14	37	72	117	170	228	292	364	>
G0V	3	5	30	23	42	133	351	695	>	>	>	>	>	>
G0V	10	0.01	1	27	50	155	388	726	>	>	>	>	>	>
G0V	10	0.01	5	>	>	>	>	>	>	>	>	>	>	>
G0V	10	0.01	15	>	>	>	>	>	>	>	>	>	>	>
G0V	10	0.01	30	>	>	>	>	>	>	>	>	>	>	>
G0V	10	1	1	0	0	0	0	0	0	0	0	0	0	0
G0V	10	1	5	1	2	5	15	29	44	61	79	99	120	320
G0V	10	1	15	41	78	253	692	>	>	>	>	>	>	>
G0V	10	1	30	430	771	>	>	>	>	>	>	>	>	>
G0V	10	5	5	0	0	0	0	0	0	0	0	0	0	0
G0V	10	5	15	2	4	12	33	61	95	133	174	216	261	650
G0V	10	5	30	23	41	126	318	598	915	>	>	>	>	>

Table 3—Continued

Table 3—Continued

MOV	10	0.01	15	>	>	>	>	>	>	>	>	>	>	>	>	>
MOV	10	0.01	30	>	>	>	>	>	>	>	>	>	>	>	>	>
MOV	10	1	1	0	0	0	0	0	0	0	0	0	0	0	0	0
MOV	10	1	5	10	16	44	90	146	201	252	296	333	364	469		
MOV	10	1	15	377	643	>	>	>	>	>	>	>	>	>	>	>
MOV	10	1	30	>	>	>	>	>	>	>	>	>	>	>	>	>
MOV	10	5	5	0	0	0	0	0	0	0	0	0	0	0	0	0
MOV	10	5	15	22	38	101	208	333	447	547	626	687	736	884		
MOV	10	5	30	212	364	903	>	>	>	>	>	>	>	>	>	>
MOV	40	0.01	1	139	199	355	524	628	681	707	722	730	736	748		
MOV	40	0.01	5	>	>	>	>	>	>	>	>	>	>	>	>	>
MOV	40	0.01	15	>	>	>	>	>	>	>	>	>	>	>	>	>
MOV	40	0.01	30	>	>	>	>	>	>	>	>	>	>	>	>	>
MOV	40	1	1	0	0	0	0	0	0	0	0	0	0	0	0	0
MOV	40	1	5	5	7	14	22	29	31	34	34	35	35	37		
MOV	40	1	15	203	288	507	729	860	921	952	968	978	985	997		
MOV	40	1	30	>	>	>	>	>	>	>	>	>	>	>	>	>
MOV	40	5	5	0	0	0	0	0	0	0	0	0	0	0	0	0
MOV	40	5	15	11	16	30	48	61	68	73	75	76	78	80		
MOV	40	5	30	113	162	292	435	529	577	601	615	623	628	639		



Table 4: Flux contrasts between the intensity peaks of the planets and stars considered in Tab.3, for a fixed separation of 1 AU between the two objects. For planets characterized by intrinsic thermal emission we don't expect a significant decrement of their fluxes for larger separations; so the contrasts calculated for 1 AU can be assumed to be valid also further away from the star. This is not true for planets shining by reflected light, whose brightness strongly depends on the physical separation (see e.g. the  $1 M_J$  planet in Fig.14 at top-left).

		Mass:	$1M_J$	$5M_J$	$15M_J$	$30 M_J$
St.	Type	Age				
G0V	0.01Gyr		$1.60 \cdot 10^{-6}$	$1.08 \cdot 10^{-4}$	$6.16 \cdot 10^{-4}$	$9.33 \cdot 10^{-3}$
G0V	1Gyr		$3.71 \cdot 10^{-8}$	$9.41 \cdot 10^{-8}$	$2.34 \cdot 10^{-6}$	$2.52 \cdot 10^{-5}$
G0V	5Gyr		-	$3.71 \cdot 10^{-8}$	$1.63 \cdot 10^{-7}$	$1.31 \cdot 10^{-6}$
M0V	0.01Gyr		$1.62 \cdot 10^{-5}$	$1.12 \cdot 10^{-3}$	$6.39 \cdot 10^{-3}$	$9.68 \cdot 10^{-2}$
M0V	1Gyr		$3.71 \cdot 10^{-8}$	$6.40 \cdot 10^{-7}$	$2.39 \cdot 10^{-5}$	$2.62 \cdot 10^{-4}$
M0V	5Gyr		-	$3.77 \cdot 10^{-8}$	$1.35 \cdot 10^{-6}$	$1.32 \cdot 10^{-5}$